Monthly Notices
of the
ROYAL ASTRONOMICAL SOCIETY

MNRAS **497,** 2175–2189 (2020)
Advance Access publication 2020 July 13

doi:10.1093/mnras/staa2053

Phase-locked polarization by photospheric reflection in the semidetached eclipsing binary μ^1 Sco

Daniel V. Cotton [1,2,3]★ Jeremy Bailey [4] Lucyna Kedziora-Chudczer [3,4] and Ain De Horta[2]

[1]*Anglo Australian Telescope, Australian National University, 418 Observatory Road, Coonabarabran, NSW 2357, Australia*
[2]*Western Sydney University, Locked Bag 1797, Penrith-South DC, NSW 1797, Australia*
[3]*Centre for Astrophysics, University of Southern Queensland, Toowoomba, Qld 4350, Australia*
[4]*School of Physics, UNSW, Sydney, NSW 2052, Australia*

Accepted 2020 July 8. Received 2020 July 8; in original form 2020 March 20

ABSTRACT

We report the detection of phase-locked polarization in the bright ($m_V = 2.98-3.24$) semidetached eclipsing binary μ^1 Sco (HD 151890). The phenomenon was observed in multiple photometric bands using two different HIPPI-class (HIgh Precision Polarimetric Instrument) polarimeters with telescopes ranging in size from 35 cm to 3.9 m. The peak-to-trough amplitude of the polarization is wavelength dependent and large, ∼700 ppm in green light, and is easily seen with even the smallest telescope. We fit the polarization phase curve with a SYNSPEC/VLIDORT polarized radiative transfer model and a Wilson–Devinney geometric formalism, which we describe in detail. Light from each star reflected by the photosphere of the other, together with a much smaller contribution from tidal distortion and eclipse effects, wholly accounts for the polarization amplitude. In the past, polarization in semidetached binaries has been attributed mostly to scattering from extra-stellar gas. Our new interpretation facilitates determining masses of such stars in non-eclipsing systems.

Key words: stars: individual: μ^1 Sco – stars: binaries: close – radiative transfer – polarization – techniques: polarimetric.

1 INTRODUCTION

1.1 Phase-locked polarization in early-type binaries

Polarization phase-locked to the orbital period in an early-type binary star was first seen in the eclipsing system β Lyr in the 1960s (Serkowski 1965; Appenzeller & Hiltner 1967).[1] Two decades earlier, Chandrasekhar (1946) had shown that a net polarization would be produced in a binary system as an eclipsing star breaks the disc symmetry of its companion,[2] but that an isolated spherical star is unpolarized. Yet, in β Lyr the polarization varied smoothly outside of eclipse. Shakhovskoi (1964) proposed that electron scattering from the extended co-rotating gaseous envelopes in the system was responsible; this mechanism quickly became favoured, with other versions differing only in the configuration of the gaseous material (Ruciński 1966; Appenzeller & Hiltner 1967). When other polarimetric binaries were discovered (e.g. Pfeiffer & Koch 1973; Rudy & Kemp 1976; Kemp & Herman 1977), models based on the same basic mechanism – gaseous envelopes or streams of co-rotating electron (Thomson) scattering gas between the stars – were developed to fit the data (Brown, McLean & Emslie 1978; Rudy & Kemp 1978).

Because polarimetry includes orientation information, it can resolve orbital elements that spectroscopy and photometry together cannot. This was first realized by Shakhovskoi (1966), who, after subtracting interstellar polarization, determined the position angle of the line of nodes in a number of eclipsing systems (Shakhovskoi 1969). In the process of developing models to describe polarization in binary systems by extra-stellar gas, Rudy & Kemp (1978) and Brown et al. (1978) independently demonstrated that polarimetry could be used to determine the system's orbital inclination, and therefore the component masses in a binary system. It is only possible to determine the component masses of a spectroscopic binary when the inclination is known by other means. Usually astronomers rely on photometry from eclipsing systems for this information.

In the model of Rudy & Kemp (1978), phase-locked polarization, with a pattern repeated twice per orbit, arises principally by single scattering from optically thin extra-stellar material. So long as there is no eclipse of the scattering material, its distribution is symmetric about the orbital plane, and the photometric variability not significant, the inclination of the system is derived from the eccentricity of the elliptical trace of the polarization in a Q–U diagram. Though founded on the same assumptions, the *BMcLE model* (Brown et al. 1978) is more sophisticated; it is a complete Fourier analysis that allows the orbital inclination and moment integrals of the density distribution to be determined, even for envelopes with no symmetry about the orbital plane. In principle, this allows calculation of the scattering mass (Koch et al. 1989) and optical depth (Aspin & Simmons 1982) and permits different scattering geometries to be distinguished, though in practice there is often degeneracy (e.g. Berdyugin et al. 2018).

With few exceptions, the polarimetric binaries characterized over the subsequent 40 yr consisted of either interacting stars or those with extended envelopes. In summarizing the sources of polariza-

★ E-mail: daniel.cotton@anu.edu.au

[1] β Lyr was the first claimed polarimetric variable (Öhman 1934), but it was not until Shakhovskoi's (1962) measurements were reproduced by other observers (references within Serkowski 1965) that its variability was accepted.

[2] Referred to as either the Chandrasekhar effect or the *eclipse* effect.

© 2020 The Author(s)
Published by Oxford University Press on behalf of the Royal Astronomical Society

Downloaded from https://academic.oup.com/mnras/article/497/2/2175/5870699 by University of Southern Queensland user on 20 June 2022

tion in binary systems, Pfeiffer & Koch (1977) state 'With one exception (U Oph[3]), un-evolved binaries do not exhibit intrinsic polarization'. Overwhelmingly, the preferred mechanism to explain the polarization in these systems was electron scattering from gas shells or streams of gas entrained between the companions (e.g. Pfeiffer & Koch 1977; McLean 1980; references within Clarke 2010). Typically data variability beyond the formal errors is naturally explained by irregularities in the flow of the transfer material (Koch et al. 1989). More recently Berdyugin et al. (2016, 2018) explored different configurations and densities of the entrained gas in the semidetached binaries HD 48099 and λ Tau. Instead of the *BMcLE model*, they used a numerical scattering code, which allows the inclusion of specific scattering geometries with eclipse effects to provide tighter constraints on the distribution of the scattering material. Such models, given sufficient instrumental precision, are good at determining binary inclination, which is fairly insensitive to the gas geometry (Berdyugin et al. 2018). The position angle of the line of nodes, however, is sensitive to geometry (Berdyugin et al. 2016). This conventional interpretation of binary polarization implies that the ability of polarimetry to determine inclinations is limited to interacting stars.

In addition to the Chandrasekhar effect and scattering from extra-stellar material, there are other potential sources of phase-locked polarization in binaries. In considering the polarigenic behaviour of the semidetached u Her[4] system, Rudy & Kemp (1977) also considered (i) photospheric reflection, (ii) tidal distortion, and (iii) asymmetric temperature distribution, i.e. as induced by the *reflection effect* – a misnomer referring to the effects of the heating of one star by the other (Eddington 1926). An inceptive theoretical radiative transfer study of polarization arising from the reflection effect had been made by Collins & Buerger (1974), and this and tidal distortion were ruled out on the basis of the low temperature and small distortion of the companion. Instead, while not ruling out extra-stellar material, Rudy & Kemp (1977) favoured photospheric reflection by the primary from the secondary for u Her. This mechanism was also considered likely for at least part of the out-of-eclipse polarization of Algol by Kemp et al. (1981), who made order of magnitude estimates for it. Tidal distortion effects have since been modelled for the visible counterpart of the X-ray source Cyg X-1 (Bochkarev et al. 1986; Dolan 1992), and lately for the general case by Harrington (2006), who shows the effects to be relatively small. Bott et al. (2018) have examined the effect on a hot-Jupiter exoplanet with the same finding.

After decades of searching, observations showing the Chandrasekhar effect were reported for Algol by Kemp et al. (1983), as a secondary effect to scattering by entrained gas. Algol remains the only star the Chandrasekhar effect has been observed in. Photospheric reflection was claimed as a component of the observed polarization in HR 5110 (Barbour & Kemp 1981) and V373 Cas (Berdyugin 1998), but no other convincing examples of other dominant mechanisms were seen until Berdyugin & Harries (1999) studied the ellipsoidal binary LZ Cep. Spectroscopic data limited the amount of extra-stellar gas that could be in the system, and this was insufficient to account for the polarization through a scattering mechanism. The polarization amplitude was also greater than could be accounted for by tidal distortion or heating. They concluded that photospheric reflection was dominant. Their simple numerical model showed reflected light to be about 3 per cent of the integrated flux, but was unable to explain the wavelength dependence of the polarization. Subsequently, photospheric reflection was also considered a plausible mechanism for polarization in the HD 48099 system (Berdyugin et al. 2016).

Recently, we (Bailey et al. 2019) studied the detached ellipsoidal binary Spica. It displays the same double-peaked polarization curve typical of all the aforementioned binaries. It does not have any entrained gas, and a modified version of our polarized radiative transfer code (Cotton et al. 2017) revealed that the majority of the polarization is accounted for by photospheric reflection, with a smaller amount ascribed to tidal distortion. Importantly, the Spica model constructed from its known stellar and orbital parameters required no fitting to match the polarization amplitude – only the interstellar offsets and the line of nodes were fit. Interestingly, the modelled dependence on wavelength (Bailey et al. 2019, supplementary information) is reminiscent of that observed for LZ Cep (Berdyugin & Harries 1999).

The polarization amplitude in the Spica system is small compared to other known polarimetric binaries, about 200 ppm. However, our models (Cotton et al. 2017; Bailey et al. 2019) indicate that the amplitude will be larger in atmospheres that are hotter and/or have lower gravity – which is a noted trend in such systems (Koch et al. 1989). Photospheric reflection may therefore account for the polarization in more binary systems than presently thought.

1.2 μ^1 Sco

μ^1 Sco (Xamidimura, HR 6247, HD 151890, HIP 82514) is one of the brightest ($m_V = 2.98$, $B - V = 0.16$) Algol-type eclipsing binaries; it has a primary eclipse depth, Δm, of 0.28 (van Antwerpen & Moon 2010). It was only the third star to be recognized as a spectroscopic binary (Pickering & Bailey 1896). Drawing on decades of radial velocity and photometry, and their own observations, van Antwerpen & Moon (2010) determine the orbit to be circular with an inclination of $65.4 \pm 1.0^\circ$ and a semimajor axis of 12.90 ± 0.04 $R_\odot$, and a period of 1.4462700(5) d (identical to Maury 1920, who was the first to study it extensively), with a primary photometric minimum at ephemeris HJD 2449534.17700(9). The mass of the B1.5 V primary is found to be 8.49 ± 0.05 $M_\odot$ and the B8–B3 secondary 5.33 ± 0.05 $M_\odot$, the radius of the primary is 4.07 ± 0.05 $R_\odot$ and the secondary is 4.38 ± 0.05 $R_\odot$ (van Antwerpen & Moon 2010) – which makes it considerably oversized for its mass (Budding, Butland & Blackford 2015). A full list of parameters pertinent to the current work is given later in Section 3.

μ^1 Sco is a semidetached binary where the secondary is close to or just filling its Roche lobe (van Antwerpen & Moon 2010; Budding et al. 2015). According to Budding et al. (2015), the secondary's oversized character implies on-going late-state interactive stellar evolution, believed to be of the 'Case A' type (i.e. it's still on the main sequence), though the primary is little effected. They further note that the system is atypical for an Algol-type binary in that the components are especially close, their masses high, and the primary particularly hot. Though gas flows in Algol-type binaries are expected to be faint, van Antwerpen & Moon (2010) suggest that it may be possible to detect the gas streams between the stars in μ^1 Sco spectroscopically using Doppler tomography.

The most recent new data on μ^1 Sco was collected by Handler & Schwarzenberg-Czerny (2013), who made multiband photometric observations, including the first such in *u* band. This ultraviolet data required inclusion of the reflection effect to fit the observations within the observational errors. Handler & Schwarzenberg-Czerny (2013) were interested in the system because the primary lies in the β Cep

[3]Despite a large number of studies, the polarigenic mechanism(s) operating in the U Oph system are not certain, though most recently mass-loss via a strong stellar wind, and eruptive mass outflows due to asynchronous rotation of the components have been favoured (Eritsian et al. 1998).
[4]68 Her.

Downloaded from https://academic.oup.com/mnras/article/497/2/2175/5870699 by University of Southern Queensland user on 20 June 2022

instability strip and the secondary in the domain of slowly pulsating B-type (SPB) stars. Which is pertinent to any polarimetric study in view of Odell's (1979) prediction of polarization from non-radial pulsations. After removing the binary light-curve solution from their data, Handler & Schwarzenberg-Czerny (2013) are left with two non-white frequencies at 0.123 and 8.07 c/d with an amplitude of around 3 mmag, but an S/N ratio less than is required for detection.

Rather surprisingly, μ^1 Sco has only been observed polarimetrically in a single study. As part of a survey of early-type stars, Serkowski (1970) observed the system just twice in the *B* band at JD 2439949.19 and 2439954.24, measuring $p = 3634$ ppm, PA $= 21^\circ$ and $p = 4094$ ppm, PA $= 18^\circ$, respectively[5] (the formal error is given as 100 ppm, but is almost certainly somewhat larger). Serkowski (1970) noted the binary phases of the measurements, but otherwise made no special mention of the system, and did not include it amongst the early-type stars he considered intrinsically polarized in his conclusions.

μ^1 Sco has a wide (347 arcsec) companion, μ^2 Sco (Pipirima, HR 6252, HD 151985, HIP 82545), which has a spectral type of B2 IV and a magnitude of $m_V = 3.6$. Despite being labelled as 'Variable' in SIMBAD[6] μ^2 Sco is not considered so by most observers, and is frequently used as a constant check star in observations of μ^1 Sco (van Antwerpen & Moon 2010; Handler & Schwarzenberg-Czerny 2013). It was the subject of two unfiltered[7] polarimetric observations by van Smith (1956) giving an average $p = 4605 \pm \sim<1302$ ppm[5], PA $= 25 \pm 4^\circ$. That these values are the same as those of μ^1 Sco within error suggests that the majority of the polarization is interstellar in origin.

In this paper, we report polarimetric observations of μ^1 Sco (and μ^2 Sco) in Section 2. In Section 3, we describe polarization models, which have been developed using a similar approach to that adopted in Bailey et al. (2019). In Section 4, the model results are shown and compared to the observations. We discuss the implications of the results in Section 5 and conclude in Section 6.

2 OBSERVATIONS

Between 2017 April and 2019 October, 147 high precision polarimetric observations were made of the close binary system μ^1 Sco (HD 151890) in three different passbands. A smaller number of observations of its wide companion μ^2 Sco (HD 151985) were also made, along with observations of low and high polarization standards for calibration purposes. These observations were made using three different telescopes and two different HIPPI-class polarimeters in varying combinations. Mini-HIPPI (Bailey, Cotton & Kedziora-Chudczer 2017) was used on a 35-cm Celestron C14 telescope at UNSW Observatory, which is located on campus in an inner suburb of Sydney, Australia. HIPPI-2 (Bailey et al. 2020a) was used both on the 3.9-m Anglo Australian Telescope (AAT) located at Siding Spring Observatory, and on the 60-cm Ritchey-Chretien telescope at the Western Sydney University (WSU) Penrith Observatory. Table 1 gives a summary of the set-up for each observing run for each filter used.

[5]The data in the source material is given in polarization magnitudes and has been converted to fractional polarization.
[6]The origin of this determination is not clear.
[7]The detector used was a 1P21 photomultiplier tube, which depending on the model and operating temperature has a peak efficiency at ∼450 nm, but has some sensitivity between 300 and 650 nm.

HIPPI-2 and Mini-HIPPI were both used in the study of the Spica binary system (Bailey et al. 2019). HIPPI-2 has also recently been used in the study of the rapidly rotating system α Oph (Bailey et al. 2020b), the red supergiant Betelgeuse (Cotton et al. 2020a), and the polluted white dwarf G29-38 (Cotton et al. 2020b).

All the observations used Hamamatsu H10720-210 photomultiplier tubes for detectors. The μ^1 Sco observations were made either without a filter (Clear) or using Astrodon SDSS g' or r' filters. Used without a filter, Mini-HIPPI and HIPPI-2 have sensitivity between ∼350 and 700 nm, resulting in a similar effective wavelength to the SDSS g' filter. The formal error for each observation is the square root of the sum of the squares of the internal measurement precision and a positioning error. The positioning error, which is different in different filter bands and on different telescopes is described in Bailey et al. (2020a). In order to beat seeing noise, HIPPI-class polarimeters use ferroelectric liquid crystals (FLCs) to modulate the sign of polarization at a frequency of 500 Hz. Three different FLCs were utilized as outlined in Table 1; their performance characteristics are described in Bailey et al. (2020a). Standard observing procedures and reduction, as described in Bailey et al. (2015, 2017, 2020a) were used, except that we are now calculating airmass to two decimal places, for improved precision on higher polarization objects. We have also improved the bandpass model for the Celestron C14 by including the transmission of the corrector plate, which is modelled as 5.49 mm MgF_2-coated iron float glass. For the purposes of the bandpass model, μ^1 Sco is modelled as spectral type B1 and μ^2 Sco as B2. For most observations, a single sky (S) measurement was made adjacent to each target (T) measurement at each of the four position angles, PA $= 0, 45, 90, 135^\circ$, in the pattern TSSTTSST. During twilight when necessary the first or last target measurement was sometimes bracketed between two skies to account for the rapid changes in sky polarization.

A small polarization due to the telescope mirrors, TP, shifts the zero-point offset of our observations. This is corrected for by reference to the straight mean of several observations of low polarization standard stars, details of which are given either in Bailey et al. (2020a) or in the caption of Table 2. Similarly, the position angle (PA) is calibrated by reference to literature measurements of high polarization standards, also given in either Bailey et al. (2017, 2020a) or in the caption of Table 1. TP calibrations are made in the same band as the observations, while the PA calibration is initially made with observations in SDSS g' and Clear, with corrections applied for other bands based on a smaller number of observations. Correction of a minor software glitch that sometimes induced a 0.3° PA error has improved the PA precision in later runs for HIPPI-2 over what was reported in Bailey et al. (2020a).

Fig. 1 displays the μ^1 Sco observations, which are also listed in Table 2. The tabulated phases have been computed based on the ephemeris of van Antwerpen & Moon (2010) (see also Section 1.2).

The right-hand panel of Fig. 1 shows the data plotted on a *Q*–*U* diagram. An approximately elliptical locus of points is traced out here in each of the three filter bands, which is the shape expected from an intermediately inclined system. The three loops are offset from each other, as one would expect if the zero-points are constant but different, as in the case of them being set by interstellar polarization. The r' data clearly has a tighter loop (i.e. a lower polarization amplitude) than g' or Clear data. This is what we expect for a reflection mechanism (Bailey et al. 2019, supplementary information). Compared to Spica, the peak-to-trough amplitude is about four times larger. Given the comparative temperatures of the components of the binaries and the shorter orbital period

Downloaded from https://academic.oup.com/mnras/article/497/2/2175/5870699 by University of Southern Queensland user on 20 June 2022

Table 1. Summary of Mini-HIPPI and HIPPI-2 observing runs.

Run	JD range	Telescope and instrument set-up[a]						Observations[b]				TP[c]		σ_{PA}[d]
	2450000 +	Instr.	Tel.	*f*/	Fil.	Mod.	Ap. (arcsec)	*n*	Exp. (s)	Dwell (s)	λ_{eff} (nm)	Eff. (per cent)	*q* (ppm)	*u* (ppm)	(°)
MC1	7871–7898	M-HIPPI	UNSW	11	Cl	MT	58.9	34	800	1595 ± 167	453.1 ± 2.0	74.0 ± 0.8	− 69.8 ± 2.9	− 10.9 ± 2.9	0.23
MC2	8017–8049	M-HIPPI	UNSW	11	Cl	MT	64.3	31	800	1746 ± 301	456.1 ± 2.9	75.2 ± 1.1	− 73.6 ± 8.8	− 20.7 ± 8.6	0.52
AC1	8153	HIPPI-2	AAT	15	Cl	BNS-E3	16.8	2	400[E]	618 ± 233	454.2 ± 0.3	67.1 ± 0.1	− 185.6 ± 1.0	8.6 ± 0.9	–
AC2	8154	HIPPI-2	AAT	15	Cl	BNS-E3	16.8	1	200	448	454.0	67.0	− 175.2 ± 0.8	14.0 ± 0.8	–
AC3	8211–8216	HIPPI-2	AAT	8*	Cl	BNS-E3	11.9	6	160	405 ± 43	457.6 ± 0.1	69.7 ± 0.0	113.3 ± 0.7	3.9 ± 0.9	0.26
MC3	8343–8344	M-HIPPI	UNSW	11	Cl	MT	64.3	6	400	1434 ± 615	452.5 ± 1.4	73.7 ± 0.6	− 56.4 ± 1.9	16.2 ± 1.9	0.54
AC4	8360–8361	HIPPI-2	AAT	8*	Cl	BNS-E7	11.9	9	320[E]	650 ± 159	459.0 ± 0.7	50.4 ± 0.3	− 10.1 ± 0.9	3.8 ± 0.9	0.86
AC5	8590–8605	HIPPI-2	AAT	15	Cl	ML-E1	12.7	7	160[E]	602 ± 353	449.6 ± 1.6	80.7 ± 0.4	− 14.2 ± 0.8	− 3.7 ± 0.7	0.27
AG1	8593–8605	HIPPI-2	AAT	15	g'	ML-E1	12.7	8	160[E]	409 ± 40	458.1 ± 0.6	92.9 ± 0.0	− 14.2 ± 0.8	− 2.6 ± 0.7	0.27
WG1	8662–8665	HIPPI-2	WSU	10.5*	g'	ML-E1	58.9	4	800	1256 ± 160	458.6 ± 1.0	93.0 ± 0.0	− 4.6 ± 3.8	3.1 ± 3.9	0.09
AG2	8669–8678	HIPPI-2	AAT	15	g'	ML-E1	12.7	11	320[E]	650 ± 118	458.1 ± 0.5	92.9 ± 0.1	− 14.5 ± 1.1	5.0 ± 1.0	0.08
WG2	8704–8707	HIPPI-2	WSU	10.5*	g'	ML-E1	58.9	6	800	1293 ± 183	458.6 ± 0.5	93.0 ± 0.0	− 32.6 ± 3.9	11.6 ± 3.8	0.05
WG3	8718–8720	HIPPI-2	WSU	10.5*	g'	ML-E1	58.9	5	800	1145 ± 17	459.2 ± 0.9	93.0 ± 0.0	− 32.6 ± 3.9	11.6 ± 3.8	0.18
WG4	8759	HIPPI-2	WSU	10.5*	g'	ML-E1	58.9	1	800	1135	459.6	93.0	1.8 ± 2.2	1.2 ± 2.1	0.44
WG5	8779–8782	HIPPI-2	WSU	10.5*	g'	ML-E1	58.9	5	800	1131 ± 11	461.7 ± 1.1	93.0 ± 0.0	1.8 ± 2.2	1.2 ± 2.1	0.61
AR1	8590–8602	HIPPI-2	AAT	15	r'	ML-E1	12.7	10	320[E]	690 ± 118	601.2 ± 0.0	62.0 ± 0.0	− 0.7 ± 2.3	14.1 ± 2.4	0.40
AR2	8669–8678	HIPPI-2	AAT	15	r'	ML-E1	12.7	7	480[E]	904 ± 368	601.2 ± 0.1	62.0 ± 0.0	− 7.0 ± 6.9	− 23.9 ± 7.1	–

Note. An asterisk indicates use of a 2× negative achromatic lens effectively making the focii *f*/16 and *f*/21 at the AAT and WSU telescope, respectively. Superscript E indicates there are a small number of exceptions to the listed dwell time.

[a]A full description along with transmission curves for all the components and modulation characterization of each modulator (Mod.) in the specified performance era (En) can be found in Bailey et al. (2020a).

[b]The dwell time (Dwell), effective wavelength (λ_{eff}), and modulation efficiency (Eff.) for the set of observations are described as median ± standard deviation.

[c]TP has been calibrated as the mean of observations of the following low polarization standards made during each run, MC1: 4× HD 2151, 14× HD 48915, 6× HD 102647, 1× HD 102870, 1× HD 140573; MC2: 2× HD 2151, 1× HD 48915, 2× HD 128620J; MC3: 9× HD 48915, 3× HD 128620J; AC1, AC2, AC3, and AC4: given in Bailey et al. (2020a) as runs 2018FEB-B, 2018FEB-D, 2018MAR, and 2018AUG, respectively; AC5: 3× HD 48915, 3× HD 102647, 1× HD 140573; AG1: 4× HD 48915, 3× HD 102647, 2× HD 128620J, 1× HD 140573; AG2: 3× HD 2151, 3× HD 102647; WG1: 4× HD 102647, 4× HD 128620J; WG2 and WG3: 1× HD 2151, 1× HD 10700, 5× HD 128620J, 1× HD 140573; WG4 and WG5: 4× HD 48915, 2× HD 128620J.

[d]Shown is the standard deviation of PA calibration observations with respect to their literature values (see Bailey et al. 2020a). PA has been calibrated as the mean of observations of the following high polarization standards made in SDSS g' or Clear during each run, MC1: 2× HD 84810, 1× HD 147084; MC2: 1× HD 147084, 1× HD 187929; MC3: 3× HD 147084, 2× HD 149757; AC1: 1× HD 80558; AC2: 1× HD 80558; AC3: 1× HD 80558, 1× HD 111613, 1× HD 147084, 1× HD 187929; AC4: 3× HD 147084, 3× HD 160529, 5× HD 187929 (which were then modified according to $\Delta PA = -4.96338 \times 10^{-2}\lambda_{eff}^2 + 4.278\lambda_{eff} - 915.5$ which is a fit to the standard observations made in SDSS g', 500SP – 1× HD 147084, 2× HD 160529, 2× HD 187929 – and 425SP – 1× HD 147084, 2× HD 160529, 2× HD 187929); AC5, AG1: 1× HD 80558, 1× HD 111613, 2× HD 147084, 1× HD 187929; WG1: 10× HD 147084, 1× HD 154445; AG2: 4× HD 147084, 1× HD 154445; WG2: 1× HD 147084, 1× HD 187929; WG3: 1× HD 147084, 1× HD 187929; WG4: 1× HD 147084, 1× HD 187929; WG5: 1× HD 160529, 2× HD 187929. The initial PA determinations for AR1 and AR2 are those for AG1 and AG2; a correction was carried out for SDSS r' based on a smaller number of standard observations made in the same band, AR1: 1× HD 147084, 1× HD 187929 (offset 1.58°); AR2: 1× HD 147084 (offset −1.39°); tabulated values are for these observations.

of the μ^1 Sco system, this is also consistent with photospheric reflection.

2.1 Statistical analysis

We examined the variability of our polarimetric data set with a moment analysis in Table 3, as is often done before looking at phases (Brooks et al. 1994; Clarke 2010). The data has been divided up by filter. In the case of the Clear observations, we also split the data by instrument, since the bandpass with HIPPI-2 varied a bit depending on the modulator condition and whether or not the Barlow lens had to be used. It is important to note here that while differences in the modulation efficiency curve for the modulators do not affect the effective wavelength, they do result in different weightings for different wavelengths to the measured polarization; this is important for the later eras of the BNS performance (see Bailey et al. 2020a).

The Error Variance is a measure of polarimetric variability not accounted for by known uncertainties; in Table 3 it has values between ∼165 and ∼335 ppm. Which confirms what is already obvious in Fig. 1 – that there is intrinsic variability in the system.

There is also a significant negative skewness in the *u* Stokes parameter in the g' and r' data (and less significantly in *q*). Which means that the tail of the distribution is on the left of the *Q*–*U* plot. Skewness can indicate an intermediate inclination of the orbit in a binary system, with its sign dependant on the position angle of the line of nodes.

At first glance it does not appear the Clear data has the same characteristics as g' and r' in Table 3, but interrogating the data more closely reveals it is consistent. The AC4 run observations were all made in quick succession, and have similar phase (Table 2); these corresponded to a period of heavy cloud when observing other targets was not possible. They also taken during the BNS modulator's Era 7, which has the most extreme drift in λ_0. When we remove this data, and the three points from AC1 and AC2 during HIPPI-2's commissioning, where modifications to the back-end of the instrument were being made on the fly, and just use data from AC3 and AC5 the anomaly disappears. Similarly there is an obvious outlier in the Mini-HIPPI data at JD = 2458039.9178 (see Fig. 1), if we remove it this data is also consistent.

2.2 μ^2 Sco

In order to obtain an estimate to the interstellar polarization of μ^1 Sco independent of our modelling, we also made measurements of its wide companion μ^2 Sco. Two Mini-HIPPI observations were obtained during the MC1 run, and an HIPPI-2 observation each in g' and r' in AG1 and AR1, respectively. A HIPPI-2 observation in Clear was made during run AC5. The same calibrations in TP and PA were applied as were for μ^1 Sco, and the other details of the observations are the same too. The results of the observations are shown in Table 4. The tabulated results probably underestimate the errors for the Mini-HIPPI observations, perhaps by a factor of 2, or 3 at most. μ^2 Sco is not as bright as the low polarization objects used to estimate the errors on the C14 at UNSW, and variability in sky conditions will be more significant.

The polarizations measured for μ^2 Sco are similar to (but not the same as) the mean values given for μ^1 Sco in Table 3, suggesting that the majority of the constant polarization is interstellar in origin.

Downloaded from https://academic.oup.com/mnras/article/497/2/2175/5870699 by University of Southern Queensland user on 20 June 2022

Table 2. High precision polarimetric observations of μ^1 Sco.

HJD 2450000 +	Phase	Run	$\lambda_{\rm eff}$ (nm)	Eff (per cent)	q (ppm)	u (ppm)	HJD 2450000 +	Phase	Run	$\lambda_{\rm eff}$ (nm)	Eff (per cent)	q (ppm)	u (ppm)
7871.99062	0.04637	MC1	456.2	75.2	2968.5 ± 31.4	2399.6 ± 31.9	8344.00325	0.41187	MC3	451.7	73.4	2769.2 ± 43.6	2599.6 ± 42.5
7872.01282	0.06172	MC1	454.4	74.5	2927.6 ± 31.1	2365.4 ± 30.8	8360.94916	0.12885	AC4	458.2	50.0	3425.4 ± 10.6	2590.2 ± 8.6
7881.03107	0.29725	MC1	452.4	73.6	2905.7 ± 29.2	3114.1 ± 29.1	8360.95832	0.13518	AC4	458.4	50.1	3431.3 ± 10.5	2616.1 ± 13.8
7881.05098	0.31101	MC1	451.6	73.3	2883.6 ± 29.3	3071.8 ± 28.3	8360.96612	0.14058	AC4	458.6	50.2	3460.6 ± 21.7	2722.6 ± 17.6
7881.93520	0.92239	MC1	459.6	76.6	2698.6 ± 32.5	2469.0 ± 32.8	8360.97692	0.14804	AC4	458.9	50.3	3532.6 ± 31.3	2773.2 ± 21.7
7881.95598	0.93676	MC1	457.1	75.6	2657.3 ± 33.7	2506.2 ± 33.7	8360.98402	0.15295	AC4	459.0	50.4	3423.5 ± 17.5	2866.3 ± 20.3
7881.97747	0.95162	MC1	455.0	74.8	2647.0 ± 32.0	2385.9 ± 32.3	8360.99097	0.15776	AC4	459.3	50.5	3472.0 ± 25.2	2814.6 ± 23.7
7881.99841	0.96610	MC1	453.7	74.2	2721.2 ± 32.7	2463.9 ± 30.9	8360.99798	0.16261	AC4	459.6	50.7	3438.8 ± 11.8	2816.7 ± 16.7
7882.02274	0.98292	MC1	452.6	73.7	2715.4 ± 33.5	2386.7 ± 31.6	8361.00492	0.16740	AC4	459.8	50.8	3356.0 ± 8.3	2877.5 ± 10.2
7884.00376	0.35267	MC1	453.2	74.0	2837.6 ± 30.5	2881.1 ± 30.5	8361.01208	0.17235	AC4	460.1	51.0	3610.3 ± 11.5	2876.7 ± 9.7
7884.05100	0.38533	MC1	451.4	73.2	2758.5 ± 30.4	2694.0 ± 30.0	8391.89104	0.52311	MC3	452.5	73.7	2890.4 ± 43.4	2381.2 ± 43.2
7888.98350	0.79583	MC1	453.5	74.1	3086.7 ± 35.1	2812.7 ± 32.7	8391.91995	0.54310	MC3	453.9	74.3	2865.9 ± 45.5	2307.9 ± 47.2
7889.05586	0.84586	MC1	451.0	73.1	2918.3 ± 30.1	2812.7 ± 31.2	8391.93471	0.55331	MC3	454.8	74.7	3012.8 ± 44.1	2383.2 ± 44.1
7889.94768	0.46249	MC1	455.8	75.1	2795.5 ± 34.7	2303.9 ± 32.5	8590.30862	0.71574	AC5	449.1	80.6	3271.1 ± 4.4	3052.0 ± 4.5
7889.96742	0.47614	MC1	454.3	74.5	2829.2 ± 31.9	2252.3 ± 32.7	8590.31604	0.72087	AR1	601.2	62.0	3431.8 ± 16.6	3060.3 ± 16.6
7889.98848	0.49070	MC1	453.2	74.0	2915.4 ± 31.8	2239.8 ± 32.2	8591.17797	0.31683	AC5	448.6	80.4	2933.0 ± 4.5	3107.2 ± 4.3
7890.00577	0.50266	MC1	452.4	73.6	2923.5 ± 31.7	2154.4 ± 31.4	8591.18550	0.32204	AR1	601.1	62.0	3162.1 ± 15.5	3059.8 ± 15.1
7890.02198	0.51387	MC1	451.8	73.4	3081.1 ± 33.4	2179.8 ± 31.7	8592.31415	0.10243	AC5	449.3	80.6	3220.8 ± 5.6	2521.3 ± 5.1
7890.03894	0.52559	MC1	451.3	73.2	3067.3 ± 32.2	2168.8 ± 31.6	8593.08740	0.63708	AC5	450.3	80.8	3354.6 ± 5.4	2739.7 ± 5.3
7890.05405	0.53604	MC1	451.0	73.1	2915.0 ± 31.9	2223.5 ± 31.2	8593.09386	0.64155	AR1	601.2	62.0	3521.2 ± 16.5	2812.0 ± 15.8
7890.95544	0.15929	MC1	454.9	74.7	3363.2 ± 42.0	2544.7 ± 41.4	8593.10075	0.64631	AG1	458.0	92.9	3253.2 ± 5.4	2604.0 ± 4.7
7890.97404	0.17215	MC1	453.7	74.2	3336.9 ± 50.3	2709.7 ± 48.3	8594.24926	0.44043	AG1	457.6	92.9	2644.6 ± 4.6	2404.6 ± 4.8
7897.02441	0.35558	MC1	451.2	73.2	2824.5 ± 29.7	2806.1 ± 30.1	8594.25570	0.44488	AR1	601.1	62.0	3028.8 ± 18.3	2610.0 ± 17.2
7897.93913	0.98805	MC1	454.7	74.6	2927.8 ± 33.8	2286.0 ± 36.5	8594.30703	0.48038	AG1	457.8	92.9	2739.3 ± 4.6	2272.3 ± 4.9
7897.95640	0.99999	MC1	453.6	74.2	2960.0 ± 33.8	2226.9 ± 34.0	8594.31308	0.48455	AR1	601.2	62.0	3121.3 ± 16.5	2510.4 ± 17.6
7897.97432	0.01238	MC1	452.8	73.8	2962.9 ± 34.0	2165.7 ± 32.7	8594.31964	0.48909	AC5	449.6	80.7	2858.9 ± 5.6	2440.5 ± 5.4
7897.99187	0.02452	MC1	452.1	73.5	3018.8 ± 33.4	2168.9 ± 33.3	8595.30705	0.17182	AR1	601.2	62.0	3435.0 ± 46.4	2840.3 ± 46.7
7898.00961	0.03678	MC1	451.6	73.3	3034.4 ± 32.1	2172.3 ± 32.9	8597.31539	0.56045	AR1	601.2	62.0	3326.1 ± 15.6	2531.9 ± 25.9
7898.02750	0.04915	MC1	451.1	73.1	3111.1 ± 32.4	2237.0 ± 32.1	8599.06394	0.76946	AC5	450.5	80.9	3129.0 ± 7.2	3048.9 ± 6.4
7898.04537	0.06151	MC1	450.7	73.0	3126.9 ± 31.5	2250.0 ± 30.9	8599.07006	0.77369	AG1	458.2	93.0	2926.4 ± 5.7	2908.3 ± 6.8
7898.06416	0.07450	MC1	450.5	72.9	3128.2 ± 28.7	2300.1 ± 31.4	8599.07705	0.77853	AR1	601.2	62.0	3335.9 ± 18.2	3027.1 ± 17.8
7898.95496	0.69043	MC1	453.6	74.2	3351.9 ± 31.2	2620.4 ± 30.7	8599.32386	0.94918	AG1	458.1	92.9	2651.8 ± 5.2	2395.5 ± 4.4
7898.97399	0.70359	MC1	452.7	73.8	3456.7 ± 30.1	2761.1 ± 29.0	8599.32952	0.95309	AR1	601.2	62.0	3096.3 ± 17.3	2598.6 ± 16.9
7898.99364	0.71718	MC1	452.0	73.5	3400.0 ± 29.3	2730.5 ± 30.1	8601.31700	0.32730	AG1	458.1	92.9	2811.2 ± 4.3	2910.3 ± 4.5
8013.90879	0.17340	MC2	451.8	73.4	3340.5 ± 31.2	2778.2 ± 31.1	8602.31569	0.01783	AR1	601.2	62.0	3123.0 ± 17.9	2595.4 ± 17.7
8013.93267	0.18991	MC2	452.8	73.8	3334.8 ± 30.9	2871.8 ± 31.6	8602.32331	0.02310	AG1	458.2	92.9	2845.4 ± 5.2	2214.6 ± 5.5
8013.95519	0.20548	MC2	453.8	74.3	3190.9 ± 31.3	2881.6 ± 34.0	8605.98606	0.55565	AG1	459.6	93.0	2950.7 ± 7.2	2259.4 ± 5.2
8016.89170	0.23588	MC2	451.6	73.3	3234.2 ± 32.0	3021.4 ± 32.3	8605.99358	0.56085	AC5	453.4	81.5	3113.1 ± 12.1	2383.0 ± 9.4
8016.93931	0.26880	MC2	453.4	74.1	3137.0 ± 34.1	3029.4 ± 33.1	8662.04050	0.31358	WG1	458.4	93.0	2843.7 ± 17.9	2928.8 ± 15.7
8016.95877	0.28226	MC2	454.6	74.6	3157.4 ± 34.0	3047.4 ± 35.1	8663.95434	0.63688	WG1	458.6	93.0	3228.6 ± 17.8	2611.8 ± 18.2
8016.97699	0.29486	MC2	456.1	75.2	3037.0 ± 38.6	3182.2 ± 37.1	8665.00634	0.36427	WG1	458.4	93.0	2699.7 ± 16.7	2812.8 ± 16.7
8016.99567	0.30777	MC2	458.1	76.0	2971.9 ± 40.3	3024.7 ± 43.0	8669.12883	0.21470	AG2	458.1	92.9	3099.3 ± 4.0	2840.8 ± 3.5
8027.88105	0.83429	MC2	452.3	73.6	2951.0 ± 31.9	3035.6 ± 32.9	8669.13804	0.22107	AR2	601.2	62.0	3501.5 ± 14.2	3105.6 ± 14.2
8027.90347	0.84979	MC2	453.2	74.0	2828.7 ± 31.6	2766.4 ± 31.2	8669.85122	0.71418	AG2	458.6	93.0	3233.2 ± 3.4	2711.4 ± 3.3
8027.92614	0.86547	MC2	454.5	74.5	2815.4 ± 32.6	2749.4 ± 32.7	8670.86732	0.41675	AR2	601.2	62.0	3001.3 ± 19.8	2857.9 ± 27.5
8027.94636	0.87945	MC2	456.1	75.2	2838.9 ± 32.9	2691.6 ± 33.3	8670.88316	0.42770	AG2	458.1	92.9	2578.8 ± 6.2	2469.1 ± 3.3
8027.97027	0.89598	MC2	458.8	76.2	2799.4 ± 35.4	2766.7 ± 34.4	8673.00108	0.89210	AG2	457.5	92.9	2666.1 ± 4.2	2543.1 ± 3.8
8039.87804	0.12942	MC2	453.6	74.2	3365.6 ± 34.7	2479.1 ± 36.0	8673.16343	0.00436	AG2	458.7	93.0	2757.3 ± 4.3	2221.8 ± 4.0
8039.89730	0.14273	MC2	454.8	74.7	3272.0 ± 34.9	2690.4 ± 35.8	8673.89816	0.51238	AG2	457.9	92.9	2800.7 ± 3.7	2202.1 ± 3.6
8039.91783	0.15693	MC2	456.6	75.4	3671.7 ± 41.0	4004.5 ± 45.7	8673.90641	0.51807	AR2	601.2	62.0	3240.8 ± 14.1	2565.3 ± 14.5
8042.88333	0.20738	MC2	454.4	74.5	3344.5 ± 33.1	3267.6 ± 32.9	8674.15167	0.68766	AG2	458.5	93.0	3128.5 ± 3.7	2685.1 ± 3.6
8042.90859	0.22484	MC2	456.5	75.4	3299.5 ± 32.3	2870.7 ± 32.9	8674.99103	0.26802	AG2	457.5	92.9	2909.2 ± 4.4	2887.2 ± 4.1
8043.88464	0.89972	MC2	454.7	74.6	2804.7 ± 34.2	2694.5 ± 34.4	8674.99758	0.27255	AR2	601.1	62.0	3379.0 ± 14.9	3127.6 ± 14.8
8043.90657	0.91488	MC2	456.6	75.4	2850.8 ± 34.7	2545.3 ± 35.5	8676.17654	0.08772	AG2	459.2	93.0	3004.0 ± 4.4	2326.6 ± 3.9
8043.92603	0.92833	MC2	458.9	76.3	2838.2 ± 37.6	2594.7 ± 36.9	8676.18606	0.09431	AR2	601.4	61.9	3409.8 ± 20.0	2694.4 ± 19.4
8044.87854	0.58693	MC2	454.5	74.5	3265.1 ± 34.8	2392.9 ± 35.3	8677.84396	0.24063	AR2	601.2	62.0	3430.7 ± 15.7	3161.3 ± 15.7
8044.89608	0.59906	MC2	455.9	75.1	3379.3 ± 34.6	2488.8 ± 34.8	8677.85367	0.24735	AG2	458.2	93.0	3021.8 ± 4.2	2881.1 ± 4.2
8044.91353	0.61112	MC2	457.7	75.8	3298.1 ± 34.5	2659.0 ± 34.7	8678.87558	0.95393	AG2	457.9	92.9	2641.8 ± 4.3	2285.4 ± 4.2
8044.93233	0.62412	MC2	460.2	76.8	3406.3 ± 36.7	2555.1 ± 37.0	8678.88456	0.96014	AR2	601.2	62.0	3100.1 ± 14.7	2609.6 ± 15.7
8047.90380	0.67869	MC2	457.6	75.8	3525.7 ± 36.8	2769.1 ± 36.8	8704.87542	0.93110	WG2	458.4	93.0	2584.6 ± 18.5	2433.2 ± 19.9
8047.92404	0.69269	MC2	460.2	76.8	3245.9 ± 37.9	2950.4 ± 37.7	8704.99069	0.01080	WG2	458.7	93.0	2752.1 ± 19.6	2202.1 ± 19.3
8047.94201	0.70512	MC2	463.8	78.1	3230.4 ± 40.5	2862.1 ± 41.7	8705.07072	0.06613	WG2	459.7	93.0	2933.6 ± 18.5	2263.1 ± 18.6
8049.88856	0.05103	MC2	456.5	75.3	3135.8 ± 34.7	2260.4 ± 34.7	8705.94277	0.66910	WG2	458.5	93.0	3193.8 ± 17.9	2663.6 ± 18.4
8049.90678	0.06363	MC2	458.6	76.2	2978.2 ± 35.5	2427.1 ± 35.2	8706.91827	0.34359	WG2	458.4	93.0	2740.5 ± 16.3	2798.7 ± 15.5
8049.92508	0.07628	MC2	461.4	77.3	3276.8 ± 38.5	2337.4 ± 37.7	8707.00354	0.40255	WG2	458.8	93.0	2498.4 ± 18.9	2611.0 ± 18.4
8153.26473	0.52881	AC1	454.4	67.1	3297.0 ± 5.4	2616.9 ± 5.0	8718.06573	0.05133	WG3	460.5	93.0	2906.1 ± 19.1	2198.2 ± 19.1
8153.27290	0.53445	AC1	454.0	67.0	3325.0 ± 6.8	2603.3 ± 6.8	8718.90832	0.63392	WG3	458.5	93.0	3242.1 ± 17.4	2538.2 ± 17.1
8154.26944	0.22350	AC2	454.0	67.0	3638.6 ± 6.8	3375.4 ± 6.3	8718.99914	0.69672	WG3	459.2	93.0	3211.8 ± 16.8	2798.6 ± 17.6
8211.31589	0.66735	AC3	457.6	69.7	3524.1 ± 6.2	2990.7 ± 6.6	8719.06301	0.74088	WG3	460.5	93.0	3038.9 ± 17.2	2855.6 ± 18.0
8212.31267	0.35655	AC3	457.6	69.7	2892.7 ± 6.1	3113.1 ± 6.2	8719.99780	0.38722	WG3	459.2	93.0	2664.9 ± 17.1	2674.5 ± 16.4
8213.30765	0.04452	AC3	457.6	69.6	3214.4 ± 6.6	2554.0 ± 6.7	8759.91091	0.98449	WG4	459.6	93.0	2744.0 ± 20.2	2313.8 ± 19.7
8214.30728	0.73570	AC3	457.6	69.7	3183.6 ± 6.6	3077.8 ± 6.0	8779.89481	0.80205	WG5	460.7	93.0	2775.5 ± 19.7	2959.4 ± 19.9
8215.31262	0.43082	AC3	457.7	69.7	2781.3 ± 7.4	2565.3 ± 6.3	8779.92552	0.82328	WG5	462.1	93.0	2757.6 ± 22.0	2914.0 ± 22.5
8216.31191	0.12176	AC3	457.7	69.7	3431.3 ± 6.8	2597.3 ± 6.3	8780.91512	0.50752	WG5	461.7	93.0	2774.9 ± 22.2	2339.6 ± 23.9
8343.97692	0.39367	MC3	451.0	73.1	2794.3 ± 44.1	2699.4 ± 44.7	8782.90202	0.88133	WG5	461.3	93.0	2596.1 ± 20.7	2786.5 ± 19.7
8343.99015	0.40281	MC3	451.3	73.2	2844.1 ± 47.0	2642.1 ± 45.6	8782.93426	0.90362	WG5	463.5	93.1	2587.2 ± 24.3	2617.8 ± 25.1

Downloaded from https://academic.oup.com/mnras/article/497/2/2175/5870699 by University of Southern Queensland user on 20 June 2022

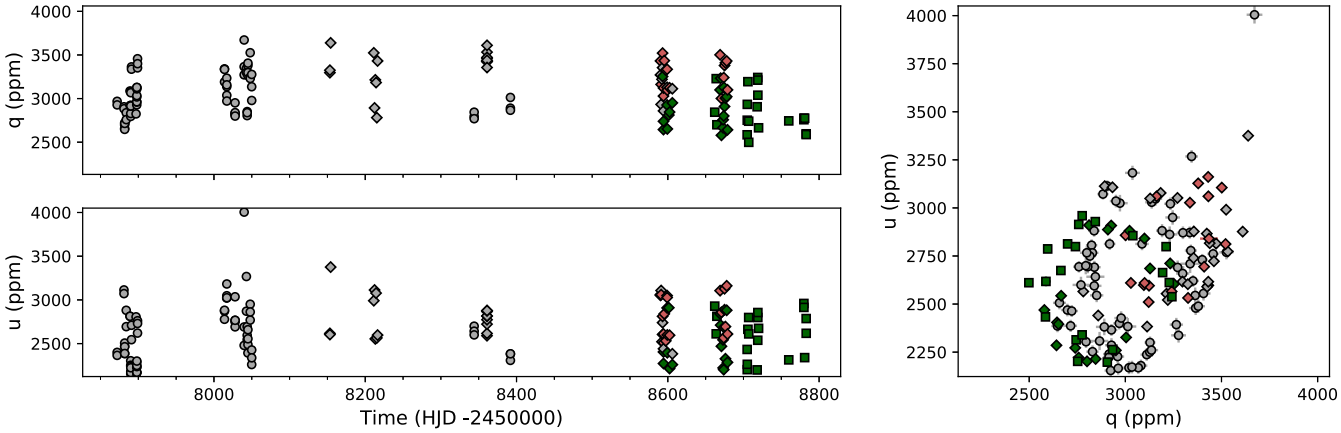

Figure 1. All polarimetric observations of μ^1 Sco (after subtraction of TP) in time series for $q = Q/I$ Stokes (top left), $u = U/I$ Stokes (bottom left), and as a Q–U diagram (right). Clear observations are in grey, SDSS g' in dark green, SDSS r' in light red, UNSW data are circles, WSU squares, and AAT diamonds.

Table 3. Moment calculations.

Filter	n	q						u					
		Mean	Mean Err.	Std. Dev.	Err. Var.	Kurtosis	Skewness	Mean	Mean Err.	Std. Dev.	Err. Var.	Kurtosis	Skewness
Clear (MH)	70	3041.5	34.6	237.5	235.0	0.164	2.223	2608.0	34.6	335.2	333.4	1.055**	5.354**
Clear (H2)	24	3278.4	10.2	222.9	222.7	0.592	2.614	2765.2	9.7	215.7	215.5	0.017	1.868
g'	38	2864.5	11.7[a]	213.4	213.1	0.180	2.072	2571.7	11.5[a]	258.1	257.9	0.002	1.514**
r'	16	3284.0	18.6	167.4	166.4	0.069	1.645*	2822.4	19.6	331.3	230.4	0.009	1.418**
Clear (MH)[b]	69	3035.2	34.5	226.9	224.2	0.082	1.908**	2596.9	34.5	292.7	290.7	0.052	2.060*
Clear (H2)[c]	12	3115.3	6.5	197.3	197.2	0.046	1.891	2766.7	6.0	277.3	277.2	0.012	1.287**

Note. MH: Mini-HIPPI, H2: HIPPI-2. Error variance (Err. Var.) is $\sqrt{(x^2 - e^2)}$, where x is the standard deviation (Std. Dev.) and e the mean error (Mean Err.) of a set of measurements; all of these quantities, along with the means are in ppm. Skewness is defined so that 3 is the normal value. The asterisks indicate significance in skewness or kurtosis (calculated using the tables of Brooks, Clarke & McGale 1994), one asterisk for 95 per cent, two for 99 per cent.
[a] g' data includes both AAT and WSU data, the mean errors of which in q/u are, respectively, 4.7/4.3 and 18.9/19.0 ppm.
[b] Data point at JD = 2458039.9178 removed.
[c] AC3 and AC5 only.

Table 4. High precision polarimetric observations of μ^2 Sco.

HJD 2450000 +	Run	$\lambda_{\rm eff}$ (nm)	Eff (per cent)	q (ppm)	u (ppm)
7872.04108	MC1	454.4	74.6	3009.8 ± 37.0	2526.3 ± 36.0
7884.03179	MC1	453.6	74.2	3169.3 ± 37.0	2413.9 ± 36.7
8596.21739	AC5	450.0	80.9	3158.0 ± 5.3	2540.5 ± 5.4
8600.31973	AR1	601.2	62.0	3452.4 ± 20.6	2796.4 ± 22.9
8601.32407	AG1	458.5	92.9	3028.2 ± 6.5	2461.6 ± 6.4

Notably the values are higher in r' than in g' or Clear, indicating a redder value of $\lambda_{\rm max}$ – the wavelength of maximum polarization – consistent with stars in the wall of the Local Hot Bubble (Cotton et al. 2019), or beyond it (Serkowski, Mathewson & Ford 1975), which have values around 550 nm.

2.3 Comparison with previous observations

For easy comparison the observations of Serkowski et al. (1975) and van Smith (1956) are given in terms of q and u in Table 5. They are probably best compared to the Mini-HIPPI observations. The observations of μ^2 Sco are in agreement within error, but this is unremarkable given the size of the errors in the old measurements. Serkowski's (1970) observations of μ^1 Sco are of the same scale as those reported here, but the agreement is at best fair when one considers the phases.

Table 5. Previous polarimetric observations of μ^1 Sco and μ^2 Sco.

Reference	Star	$\lambda_{\rm eff}$ (nm)	q (ppm)	u (ppm)	Phase
Serkowski (1970)	μ^1 Sco	∼435	2701 ± 100	2431 ± 100	0.616
Serkowski (1970)	μ^1 Sco	∼435	3312 ± 100	2406 ± 100	0.108
van Smith (1956)	μ^2 Sco	∼450	2960 ± 1302	3527 ± 1302	

3 MODELLING

The approach to modelling the polarization of a binary system follows the methods described by Bailey et al. (2019). We model only the polarization effects arising from the photospheres of the two stars, including reflection of light from one star off the other and vice versa, tidal distortion of the stars, and the eclipse effect (Chandrasekhar 1946; Kemp et al. 1983).

These methods are an extension of those we have used for modelling the polarization of rapidly rotating stars (Cotton et al. 2017; Bailey et al. 2020b). We map the distribution of temperature and gravity over the surface of the stars and interpolate in a set of stellar atmosphere models to determine the spectral radiance (specific

Downloaded from https://academic.oup.com/mnras/article/497/2/2175/5870699 by University of Southern Queensland user on 20 June 2022

intensity) and polarization of the light emitted and reflected from each point on the stellar surface. These values can then be integrated over the stars to give the total light and polarization as a function of orbital phase.

3.1 Binary geometry

The treatment of binary geometry follows the methods of Wilson & Devinney (1971) and Wilson (1979). The surfaces of the stars are modelled as equipotential surfaces in a Roche model using an extended definition of the potential Ω as given in equation (1) of Wilson (1979). We use a Cartesian coordinate system in which the centre of the primary star is at the origin, the line joining the two stars is along the x-axis and the binary orbit is in the xy-plane. Coordinates are expressed in units of the orbital semimajor axis. The methods allow for eccentric orbits and non-synchronous rotation as was the case in our modelling of Spica (Bailey et al. 2019). However, in the case of μ^1 Sco we consider only the simpler case of a circular orbit and synchronous rotation.

At a given point on the stellar surface with coordinates x, y, z, the local effective gravity is given by the vector

$$\boldsymbol{g}_{\rm eff} = \left[\partial\Omega/\partial x, \partial\Omega/\partial y, \partial\Omega/\partial z\right]. \quad (1)$$

The local normal to the surface $\boldsymbol{n}$ is in the opposite direction and thus given by

$$\boldsymbol{n} = -\boldsymbol{g}_{\rm eff}/|\boldsymbol{g}_{\rm eff}|. \quad (2)$$

If $\boldsymbol{o}$ is the normalized vector to the observer (the direction of which will depend on orbital inclination and orbital phase), then

$$\mu = \boldsymbol{n} \cdot \boldsymbol{o}, \quad (3)$$

where μ is the cosine of the local viewing zenith angle. If $\mu < 0$ then the point is on the unseen side of the star.

Our treatment of reflected light requires the direction to the source. In our geometry this vector $\boldsymbol{s}$ is

$$\boldsymbol{s} = \left[D - x, -y, -z\right], \quad (4)$$

where the source is taken to be the centre of the other star at a distance D along the x-axis, and for a circular orbit, $D = 1$ (with an eccentric orbit D would vary with orbital phase). Then

$$\mu_0 = \boldsymbol{n} \cdot (\boldsymbol{s}/|\boldsymbol{s}|), \quad (5)$$

where μ_0 is the cosine of the illuminating zenith angle. If $\mu_0 < 0$ then the point is not illuminated by the source. The angle between the plane containing $\boldsymbol{o}$ and $\boldsymbol{n}$ and that containing $\boldsymbol{s}$ and $\boldsymbol{n}$ is the azimuthal angle $\phi - \phi_0$. The three geometrical parameters μ, μ_0, and $\phi - \phi_0$ are needed as inputs for the radiative transfer calculation.

The above discussion applies to points on the surface of the primary star. The secondary star is treated in the same way by moving the coordinate system origin to the centre of the secondary and defining an internal potential according to equation (2) of Wilson (1979).

3.2 Gravity darkening

We assume that gravity and effective temperature are related by the von Zeipel law, $T_{\rm eff} \propto g^{\beta}$ with $\beta = 0.25$ (von Zeipel 1924). A recent model of gravity darkening in binary stars by Espinosa Lara & Rieutord (2012) is based on the assumption that energy flux is antiparallel to effective gravity. It shows deviations from the von Zeipel law, particularly at extreme mass ratios, but for binaries where the two stars have similar masses the effective β remains close to the von Zeipel value of 0.25. Using this relation and the Roche model we can then determine the $T_{\rm eff}$ at any point on the star's surface given the polar value.

3.3 Stellar atmosphere models

For each star we calculate a set of ATLAS9 stellar atmosphere models covering a range of $\log g$ and $T_{\rm eff}$ values appropriate for each star. The models are based on the solar composition model grids of Castelli & Kurucz (2003). Because of our assumption of the von Zeipel relationship, a set of models derived by varying one parameter ($\log g$) are sufficient to cover each star.

3.4 Polarized radiative transfer

To calculate the spectral radiance (specific intensity) and polarization of the radiation from these stellar atmosphere models, we use a version of the SYNSPEC stellar spectral synthesis code (Hubeny, Stefl & Harmanec 1985; Hubeny 2012), modified to include polarized radiative transfer using the VLIDORT code of Spurr (2006). VLIDORT (Vector Linearized Discrete Ordinate Radiative Transfer) is an implementation of the discrete ordinate method of radiative transfer, incorporating a full treatment of polarization. It has been used in Earth atmosphere research as well as planetary atmosphere modelling (Bailey, Kedziora-Chudczer & Bott 2018; Bott et al. 2018). In Cotton et al. (2017) and Bailey et al. (2020b), SYNSPEC/VLIDORT was used for modelling the polarization of a rotationally distorted star, and the supplementary materials of the first work included verifications of the methods by comparison with stellar polarization calculations of Harrington (2015) and rotating star polarization models of Sonneborn (1982).

The polarization effects included in the analysis are Thomson scattering from electrons as well as Rayleigh scattering from H, He, and H_2 all of which are described by a Rayleigh scattering matrix. Electron scattering is the main effect at the temperatures of the μ^1 Sco components.

We do separate radiative transfer calculations for the emitted light and reflected light from the star. For the emitted light, we calculate the intensity and polarization from each stellar atmosphere model as a function of wavelength and viewing angle (μ). The wavelength grid is non-uniform and is chosen by SYNSPEC to fully sample the line structure of the spectrum. We re-bin to a uniform wavelength spacing of 0.04 nm for further analysis.

For reflected light the methods are similar, but there are now three geometric parameters, the viewing zenith angle (μ), the illuminating zenith angle (μ_0), and the azimuthal angle between the two ($\phi - \phi_0$) as described in Section 3.1. We calculate intensity and polarization for each wavelength and for a coarse grid of geometric parameters (9 μ values, 9 μ_0 values, 13 azimuths) and use 3D spline interpolation in this grid to obtain values for any required geometry.

3.5 Integration over the stars

For a given inclination and orbital phase we set up a rectangular grid of pixels covering the observer's view of the star and with a grid spacing of 0.005 times the orbital semimajor axis. For each pixel that overlaps one of the stars, and is not occulted by the other star, we determine the local effective gravity (and hence the effective temperature) and the geometric parameters as described in Section 3.1. We then interpolate in the set of stellar atmosphere radiative transfer results as described in Sections 3.3 and 3.4. We interpolate first in gravity and then in geometry to obtain an intensity

Downloaded from https://academic.oup.com/mnras/article/497/2/2175/5870699 by University of Southern Queensland user on 20 June 2022

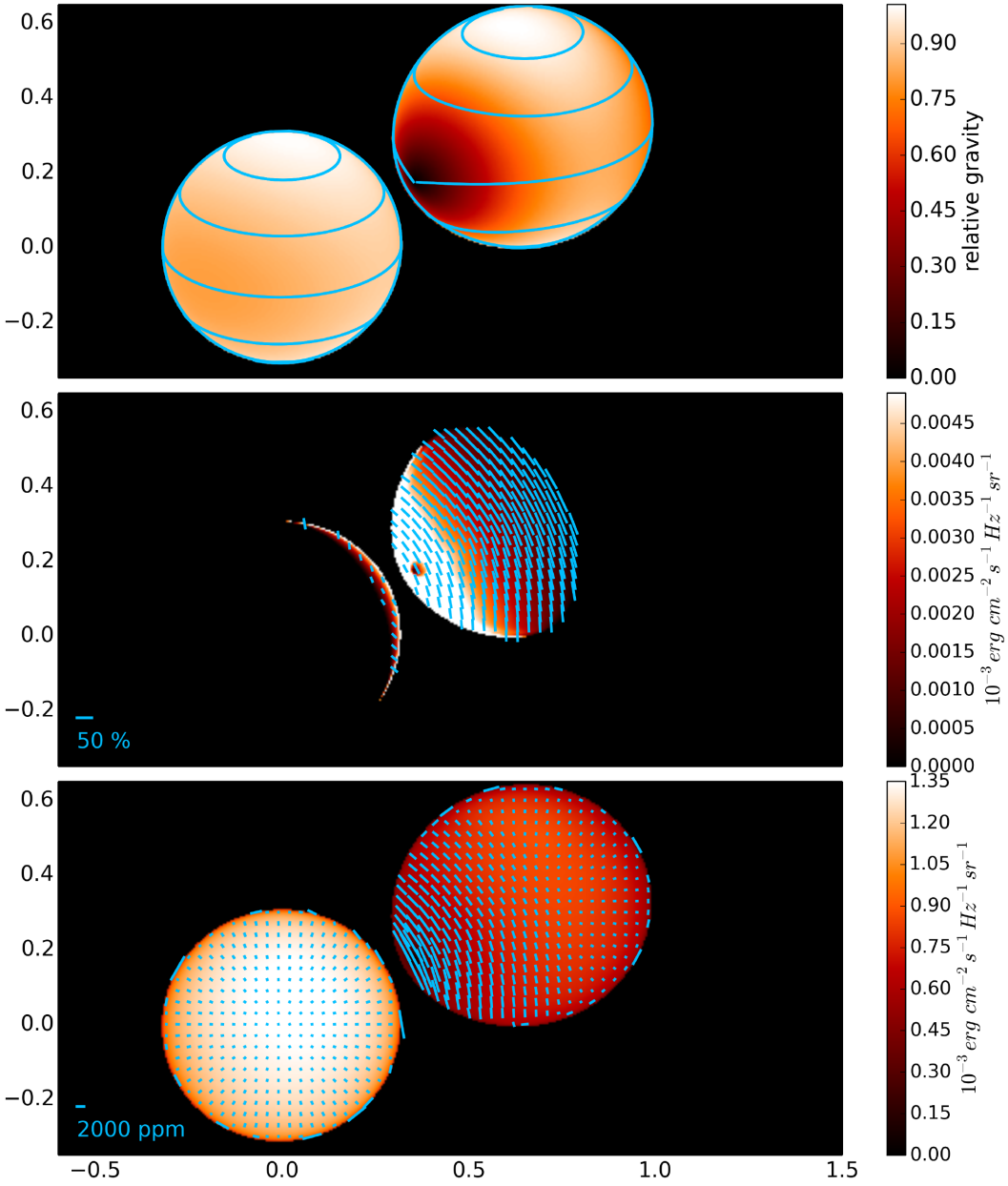

Figure 2. Example of polarization modelling of μ^1 Sco at a phase of 140° (= 0.38̇). The upper panel shows the gravity distribution of each star relative to the polar value. The middle panel shows the spectral radiance (specific intensity) overlaid with polarization vectors for the reflected light only. The lower panel is the same but including both emitted and reflected light. Intensity is plotted for every pixel, polarization vectors are plotted for every sixth pixel in each direction. These model results are for a wavelength of 450 nm.

and polarization value for each pixel. These values can be plotted on an image as in Fig. 2, or the values can be summed over the two stars to give the integrated polarization as a function of phase.

3.6 Polarization models of μ^1 Sco

Our modelling of μ^1 Sco is based on the parameters for the system determined by van Antwerpen & Moon (2010) from fitting to the light curve and radial velocity data. The parameters used as input to our modelling are listed in Table 6. We note that an alternate analysis of the system by Budding et al. (2015) gives very similar parameters. The relative geometry of the binary system is determined by the mass ratio, here denoted q_b, and the potentials of the two stars. The primary potential is as listed in Table 6 and the secondary potential is constrained by the requirement that it fills its Roche lobe (i.e. a semidetached binary as also assumed by van Antwerpen & Moon 2010). The rotation of both stars is assumed to be synchronized with the orbital period.

Our modelling code requires the polar temperature and gravity of each star as input values. The temperatures listed by van Antwerpen & Moon (2010) are mean temperatures, the polar temperatures were calculated from these allowing for the tidal distortion of the stars and assuming the von Zeipel (1924) gravity darkening law. The polar gravity is calculated from the masses listed in Table 6, the relative radii and the orbital semimajor axis as listed in the table.

Downloaded from https://academic.oup.com/mnras/article/497/2/2175/5870699 by University of Southern Queensland user on 20 June 2022

Table 6. Parameters of μ^1 Sco system used as polarization model input.

Parameter	Value	Comments
Adopted parameters from van Antwerpen & Moon (2010)		
Primary mass (M_1)	8.49 ± 0.05 M$_\odot$	
Primary $T_{\rm eff}$ (T_1)	$23\,725 \pm 500$ K	(Mean temp.)
Primary potential (Ω_1)	3.85 ± 0.01	
Secondary mass (M_2)	5.33 ± 0.05 M$_\odot$	
Secondary $T_{\rm eff}$ (T_2)	$16\,850 \pm 500$ K	(Mean temp.)
Mass ratio (q_b)	0.627 ± 0.004	
Inclination (i)	$65.4 \pm 1.0^\circ$	
Eccentricity (e)	1.0	
Semimajor axis (a)	12.90 ± 0.04 R$_\odot$	
Additional input parameters for polarization model (derived from above)		
Primary polar temp. ($T1_p$)	24 350 K	
Primary polar gravity ($\log g1_p$)	4.169 (from M_1, Ω_1, q_b, a)	
Secondary polar temp. ($T2_p$)	18 110 K	
Secondary polar gravity ($\log g2_p$)	3.939	(From M_2. q_b, a)

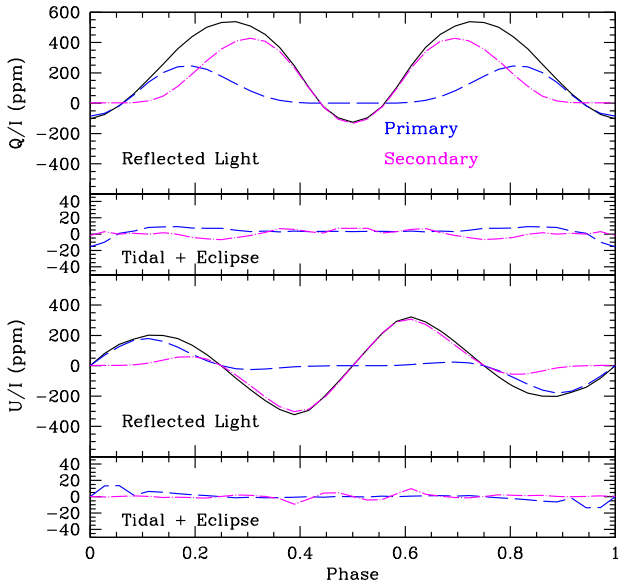

Figure 3. Components making up the total phase dependent modelled polarization of μ^1 Sco at 450 nm. Contributions from the primary component (dashed blue lines), and from the secondary (dot–dashed magenta lines) are split into the contribution of reflected light, and the thermal emission which includes the tidal and eclipse effects. All contributions are shown as a fraction of the total light from both components. The black lines show the total polarization as used in the fits in Fig. 4 (a–c).

4 RESULTS AND ANALYSIS

4.1 Modelling results

To compare our observational data with the models we have calculated them at 35 phase angles at two wavelengths – 450 and 600 nm – since the calculations are computationally very expensive. The fitted model curves include contributions from reflection, tidal distortion and an eclipse effect, all for both primary and secondary components. The break-down of these components is shown for the 450 nm case in Fig. 3.

Two features of Fig. 3 are worth noting. First, reflection is the most important effect, with tidal forces making a much smaller contribution. The magnitude of the eclipse effect is larger than the tidal forces, but still relatively small. Compared to Spica (Bailey et al. 2019), whose components are more massive but wider separated, the tidal effect is proportionally smaller in μ^1 Sco. Secondly, the contributions of both components are important, and consequently the curves have a more complicated shape than in modelled hot-Jupiter exoplanet systems (Seager, Whitney & Sasselov 2000; Bott et al. 2018).

In the 600 nm case (not shown), the phase curves look similar. However, the amplitude of the polarization from reflection is smaller – about two-thirds that of the 450 nm case. Conversely, the eclipse effect is about 50 per cent larger for the 600 nm calculation.

4.2 Model fitting

To find the best fit we use a Levenberg–Marquardt non-linear least-squares algorithm (Press et al. 1992) with just three parameters: the offsets in each of the linear polarization Stokes parameters, Z_q and Z_u, and the position angle of the line of nodes, Ω – there are no parameters that adjust the amplitude of the polarization. The results of our modelling fits to various data sets are shown in Fig. 4, and listed in Table 7 are the fitted parameters and their uncertainties (determined using a bootstrap analysis based on 1000 random samplings from the available observations).

The values of Z_q and Z_u are similar to the mean values of q and u given in Table 3, typically differing by around 100 ppm in any given band. This means they are also similar to the measured values for μ^2 Sco (Table 4), and thus represent close to the interstellar polarization values. Assuming this to be the case, the g' to r' Z_p ratio corresponds to a $\lambda_{\rm max}$ for the ISM of ∼650 nm – a little redder than the typical value of 550 nm. That the μ^2 Sco values do not agree exactly with the offset values may suggest differences in dust content on the sightlines of the two stars – and as the interstellar polarization is significant and they're a fairly wide binary this is possible. Alternatively it could indicate μ^2 Sco is intrinsically polarized. Most B-type stars are intrinsically polarized (Cotton et al. 2016), so this is also possible.

The polarization amplitude of the 600 nm model is smaller than that of the 450 nm model. There are no fit parameters that change the polarization amplitude to fit the data. Despite this, the amplitude and shape of the polarization phase curves in Fig. 4 are all very well matched by our monochromatic fits. The match to the complicated shape of the phase curves described by Fig. 3 is especially evident in q in the g' data (Fig. 4c). Any effect neglected by the model must fit within the much smaller magnitude described by the residuals – this includes scattering by gas streams. However, we believe that the largest variances can be explained by the simplifications made in the models or observational inaccuracies not captured by the formal errors; in particular difficulties around *PA* calibration.

4.2.1 Discrepancies due to systematic observational effects

An instructive example is Fig. 4(c), which shows a region around phase 0.8–0.9 in u where the g' observations deviate from the model. In Fig. 5, the residuals in this data are broken down by telescope and run, with WG5 highlighted. Run WG5 makes up most of the discrepant data at phase 0.8–0.9. It can be seen that where the model underestimates the data in u it overestimates the data in q. This suggests a difference in the position angle calibration (PA). A simple calculation shows that a 1° change in position angle corresponds to ∼100 ppm being transferred from q to u at these polarization levels.

The high polarization calibration stars we use have uncertainties of around a degree in PA (Bailey et al. 2020a). We use a short list of standards with the aim of collecting enough comparative data to improve standard precision at a later date, but this is beyond the scope of the current paper. Here, however, we can demonstrate that

Downloaded from https://academic.oup.com/mnras/article/497/2/2175/5870699 by University of Southern Queensland user on 20 June 2022

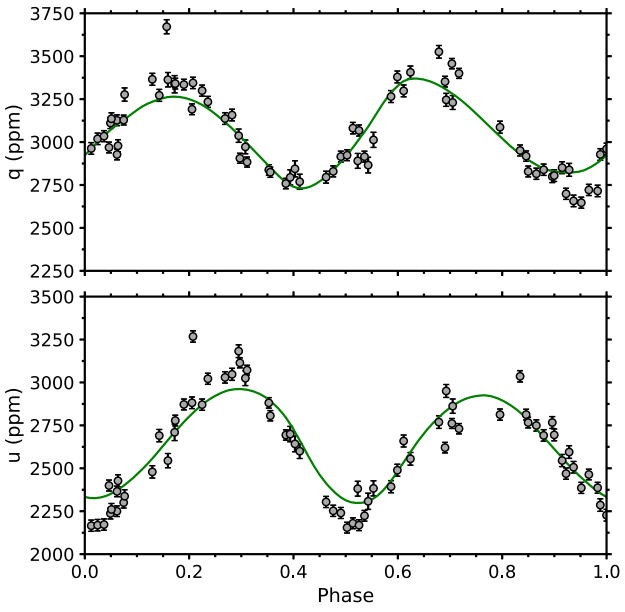

(a) Mini-HIPPI Clear data, 450 nm fit.

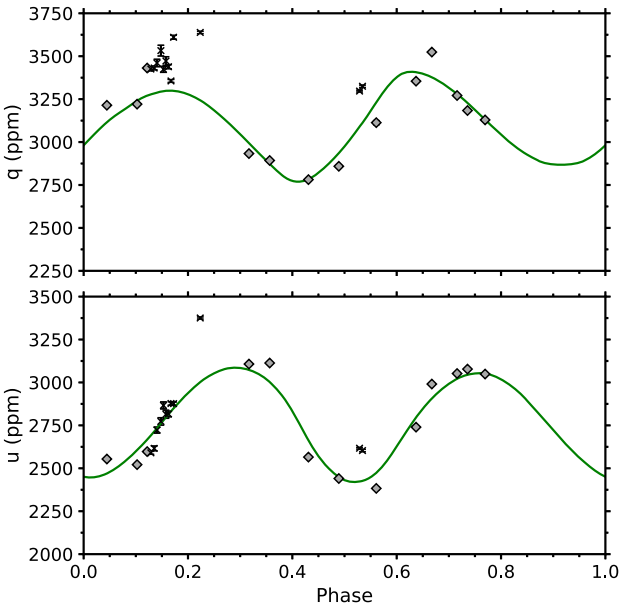

(b) HIPPI-2 Clear data, 450 nm fit.

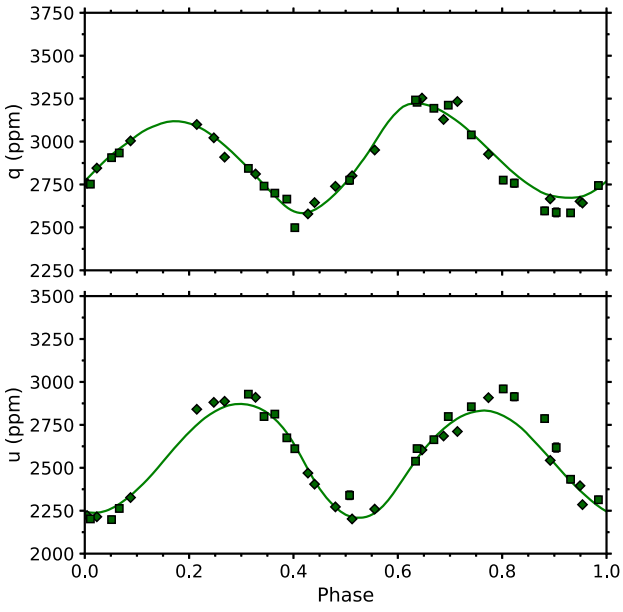

(c) HIPPI-2 g' data, 450 nm fit.

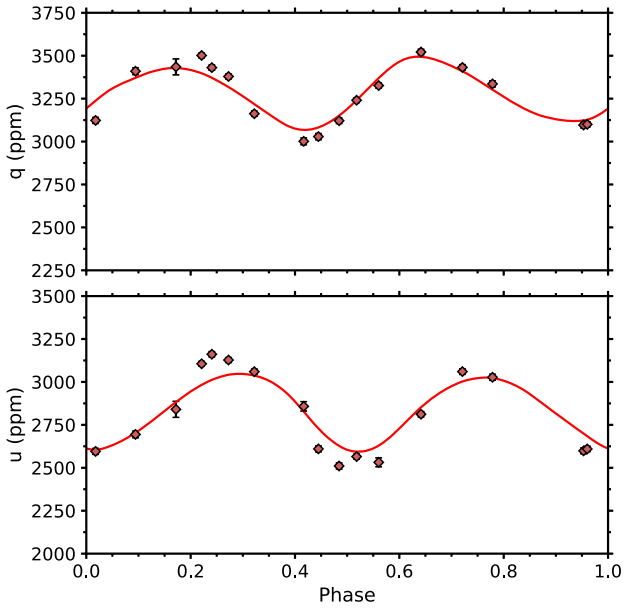

(d) HIPPI-2 r' data, 600 nm fit.

Figure 4. Polarization phase curves showing monochromatic fits (450 nm – green lines; 600 nm – red line) to different observational data. Clear observations are in grey, SDSS g' in dark green, SDSS r' in light red, UNSW data are circles, WSU squares and AAT diamonds (runs AC3 and AC5) and crosses (runs AC1, AC2, and AC4 not used for the fit. Fit curves are calculated for phase intervals of $0.02\dot{7}$ (10°) and interpolated in between.

Table 7. Fit parameters.

Filter	Z_q (ppm)	Z_u (ppm)	Ω (°)
Clear (MH)	2962.6 ± 13.2	2428.1 ± 15.2	123.84 ± 1.02
Clear (H2)[a]	3014.5 ± 30.4	2548.7 ± 18.1	125.60 ± 1.77
g'	2810.6 ± 7.4	2340.7 ± 9.5	123.21 ± 1.17
r'	3222.3 ± 13.8	2686.3 ± 24.4	124.06 ± 1.38

Note. MH: Mini-HIPPI, H2: HIPPI-2.
[a]AC3 and AC5 only.

the PA calibration is the likely cause of the observed discrepancy with Table 8. Shown in the table are the absolute PA correction for each WSU run, and the relative differences to that for each standard observation, separated by standard. Every run except WG5 used an observation of HD 147084, most also used observations of HD 187929 which comparably has a positive offset. However, WG5 includes only observations of HD 187929 and HD 160529 which shows a large positive offset relative to HD 187929. The net effect of this is that WG5 data is probably rotated by nearly a degree relative to the other runs, accounting for the discrepancy to the model. The multiple observations of HD 147084 during WG1, demonstrate that

Downloaded from https://academic.oup.com/mnras/article/497/2/2175/5870699 by University of Southern Queensland user on 20 June 2022

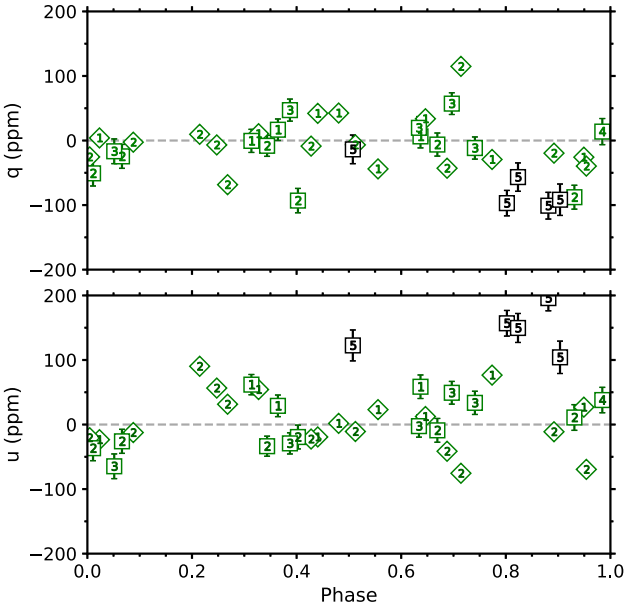

Figure 5. Residuals (data − model) from the fits to data presented in Fig. 4(c). Numbers and symbols indicate the telescope the data was taken with AAT (diamonds) and WSU (squares), and the numbers the specific run. Highlighted is run WG5 – black squares annotated '5'.

Table 8. WSU PA calibration in g'.

Run	WG1	WG2	WG3	WG4	WG5
PA Corr.	50.12	95.58	95.45	5.91	5.89
Standard	*Relative difference to PA correction*				
HD 147084	− 0.24	−0.05	−0.18	−0.44	
	+0.01				
	− 0.01				
	− 0.03				
	− 0.05				
	+0.10				
	− 0.00				
	− 0.05				
	+0.09				
	+0.11				
HD 154445	+0.08				
HD 160529					+0.84
HD 187929		+0.05	+0.18	+0.44	−0.25
					−0.59

Note. All values are in degrees. The typical error in an individual observation is 0.05° for the WG runs.

the differences between calibrator stars are significant. AAT runs typically include more observations of a greater number of standards, and these effects tend to average out, but smaller offsets will also be present between runs.

A similar issue exists for the Mini-HIPPI data presented in Fig. 4(a), where 27 out of 34 observations from run MC1 fall short of the model prediction in u. The PA calibration for MC1 includes two observations of HD 84810 which show approximately a −0.5° offset to HD 147084. Whereas MC2 and MC3 runs include standards showing a positive offset to HD 147084 (HD 187929, and HD 149757 which is ∼ + 1°. Because of the uneven sampling, the MC1 points correspond mostly to the minimums in the u curve (phases near 0.0 and 0.5). As a work-around for a wiring issue the MC1 run used different instrument PAs (−90°, −45°, 0°, 45°) to those used for later runs. The PA correction for MC1 is very close to 90°, so any inaccuracy caused by using non-standard instrument angles may be limited to one Stokes parameter.

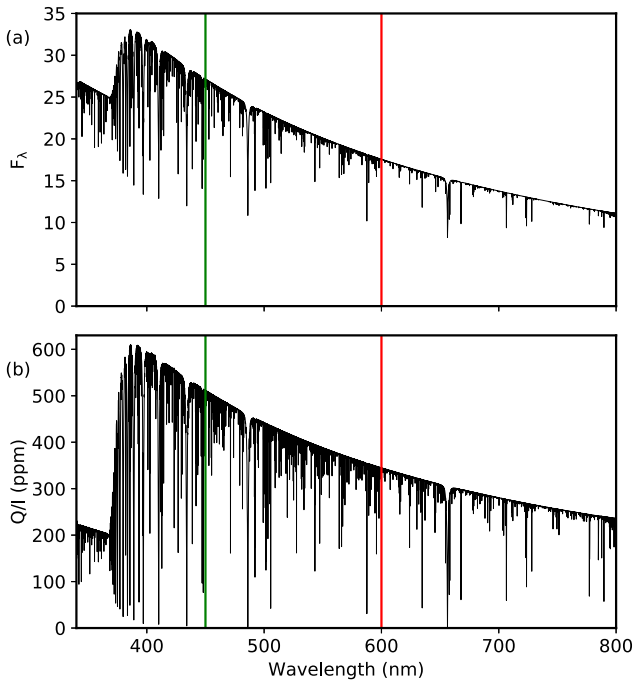

Figure 6. The flux spectrum (a) and polarization spectrum in Q/I (b) at a phase of 110° (0.3056) for the μ^1 Sco system (black). The green (450 nm) and red (600 nm) lines show the wavelengths of the monochromatic models.

Most of the calibration issues for HIPPI-2 on its commissioning runs have already described in Section 2.1. In addition to this, during early HIPPI-2 runs a minor software glitch resulted in a sporadic rotation error of ∼0.3° which amounts to ∼30 ppm being transferred between q and u. The issue was prevalent in runs AC1–4.

Given the city-based aspect of the WSU and UNSW observatories, the sky background changes more quickly close to the horizon, and is probably not as well corrected for by a sky measurement made sequentially with the target measurement. The scatter in the Mini-HIPPI measurements is greater than for other bands. It should be noted that μ^1 Sco is 1–2 magnitudes fainter than the stars used to estimate the precision of the instrument on the UNSW telescope (Bailey et al. 2020a), and the UNSW observatory is much more badly effected by light pollution than WSU. The target is also much more difficult to centre in the aperture at UNSW because of severe backlash in the C14's mount, particularly poor centring is the most likely cause of the two most discrepant individual points in the Mini-HIPPI data.

4.2.2 *Discrepancies due to broad-band effects*

Systematic errors also arise as a result of fitting monochromatic models to broad-band observations. The efficiency corrections applied by the bandpass model do not account for polarization changing as a function of wavelength, since this would require predicting the polarization before the observations are processed. However, once a model has been devised this can be fed into the bandpass model to see the effect. It is not practical to generate a polarization spectrum for the entire set of phases, but in Fig. 6(b) the polarization

Downloaded from https://academic.oup.com/mnras/article/497/2/2175/5870699 by University of Southern Queensland user on 20 June 2022

spectrum for *Q*/*I* at a phase of 110° (0.3056) is presented as an example. The polarization has a complex non-linear wavelength dependence.

Calculating the polarization using the polarization spectrum in Fig. 6(b) and the detailed flux spectrum for the system in 6(a) in our bandpass model reveals that the 450 nm model overestimates the polarization by ∼25 ppm in both the g' and Mini-HIPPI passband at airmass 1.0 – the situation is improved at higher airmasses since the lower polarization region shortward of 400 nm is attenuated – which also accounts for some of the scatter in that data, though this is less than 10 ppm. A smaller effect due to the polarization spectrum changing with the changing contributions of the binary components will also be present correlated with phase (see Fig. 3), since the spectral types are not the same.

Together the above described observational complications will account for the majority of the scatter in the data. This cannot be due to scattering from gas, as that is a grey process and not all bands are equally affected.

Smaller residuals in the g' and r' data, that might be phase dependent, do not map as easily to the phase curves. If real these probably relate to the effects of heating on the phase-locked stars which is not currently accounted for by the model. Taking account of this is the subject of future work.

4.3 Orbital orientation

The fit of the models to the data determines the position angle of the line of nodes (Ω) of the orbit as listed in Table 7. This is further illustrated in Fig. 7. Here, the polarization position angle of the g' observations, after correction for the offsets in Table 7, is compared with the modelled position angle. The dashed line shows the position angle in the model coordinate system (e.g. as used in Fig. 2) which has the orbit oriented along the *x*-axis and corresponds to $\Omega = 90°$. To fit the data the model needs to be rotated by a further 33.21° giving $\Omega = 123.21°$.

It can be seen from Fig, 7 that the position angle increases with time. Since position angle is measured anticlockwise from north, the orbital direction is therefore also anticlockwise on the sky.

5 DISCUSSION

5.1 The polarigenic mechanism

The observations of μ^1 Sco clearly show a double peaked polarization variation of the same form as seen in many other binary systems as discussed in Section 1. In the past the most common interpretation of such polarization has been that it is due to electron scattering from optically thin circumstellar gas as described, for example, by the *BMcLE model* (Brown et al. 1978).

It has been previously shown using simplified mechanisms (Berdyugin & Harries 1999; Berdyugin et al. 2016) that photospheric reflection can match the observed double-peaked structure. Moreover, our polarized radiative transfer analysis clearly shows that the observed polarization amplitude can be entirely explained by effects due to the stars' photospheres, with reflection of light being the most important effect. Indeed the model predicts the correct amplitude for the polarization using only the input parameters derived from the light curve and radial velocity model of van Antwerpen & Moon (2010). There are no adjustable fit parameters that change the polarization amplitude. The only parameters that were fitted to the data were the polarization offsets (probably due to interstellar polarization) and the orientation of the orbit.

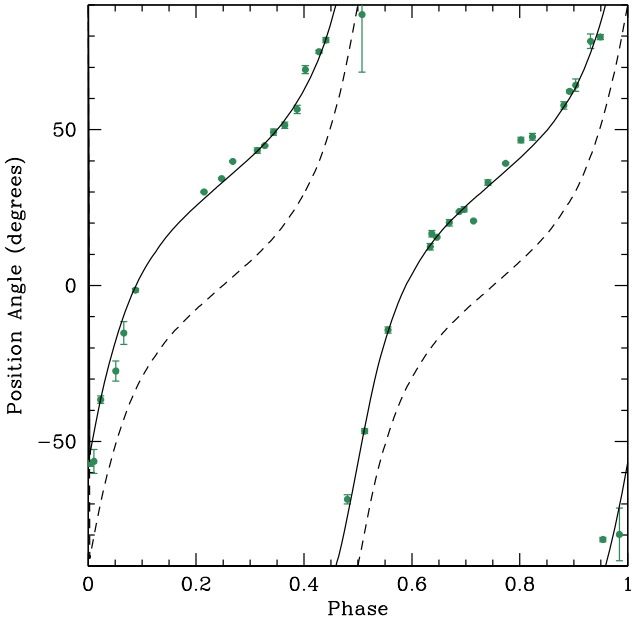

Figure 7. Polarization position angle variation shown by the g'-band data (green points) of μ^1 Sco after correcting for the polarization offsets listed in Table 7. The dashed line shows the modelled polarization position angle in the model coordinate system. Rotating the model through a further 33.21° gives the solid line which corresponds to the position angle of the line of nodes of 123.21° as given in Table 7.

As well as the correct prediction of the observed polarization amplitude in both μ^1 Sco and Spica (Bailey et al. 2019), a number of other factors support the reflection interpretation. First, the reflection model correctly predicts the polarization curve shapes that have slightly different shapes for the two maxima and the two minima with no further assumptions. Secondly, the reflection model predicts the correct wavelength dependence of the polarization amplitude, with smaller polarization amplitudes in the r' than in the g' band. The *BMcLE model* with optically thin electron scattering gas predicts a wavelength independent polarization amplitude.[8] Thirdly, the reflection model correctly predicts that polarization will be seen in both semidetached binaries such as μ^1 Sco and in detached binaries such as Spica, whereas on the *BMcLE model* we would expect polarization to occur primarily in semidetached binaries where there is mass transfer to provide a source of circumstellar gas.

It is possible that reflection accounts for a lot of the polarization observed in early-type binaries. All hot stars have electrons in their atmosphere which lead to a small (a few per cent) of incident light being reflected, and as this light is predominantly single scattered it will be very highly (∼90 per cent) polarized at optimal scattering angles (see fig. 2 of Bailey et al. 2019). The percentage of light reflected increases with increasing temperature and decreasing surface gravity. This matches the trend of increasingly large intrinsic polarizations found in more luminous early-type binary systems (Koch et al. 1989),[9] which implies (Schaffer 2015) photospheric reflection is a more prominent mechanism than has been credited.

[8] Berdyugin et al. (2016) explain a wavelength dependence in HD 48099 by a dilution effect of unpolarized free–free emission from the surrounding circumstellar matter.

[9] An extreme example is the 8000 ppm amplitude seen in the O8.5I + O7IIIf binary HD 149404 (Luna 1988).

Downloaded from https://academic.oup.com/mnras/article/497/2/2175/5870699 by University of Southern Queensland user on 20 June 2022

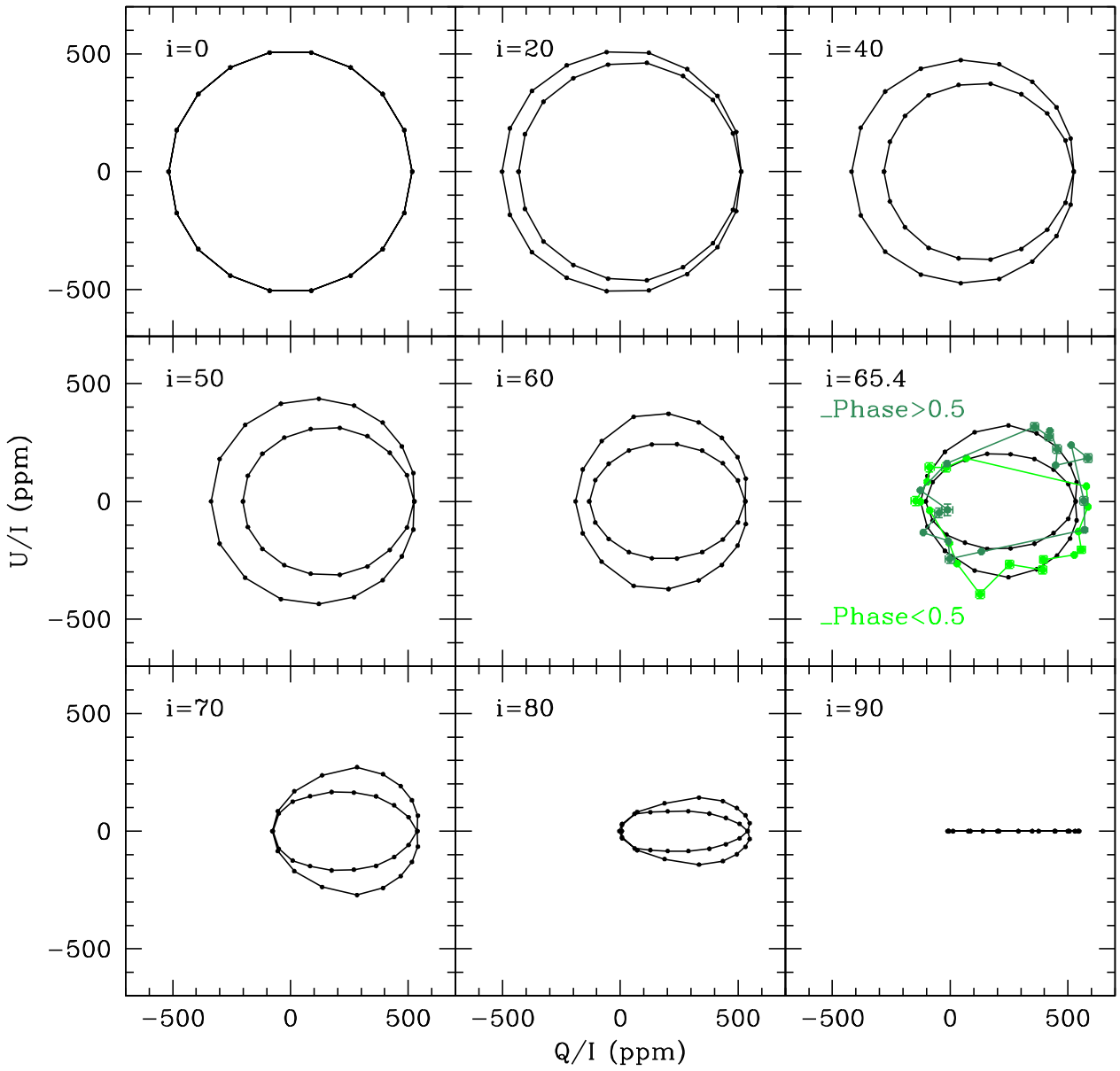

Figure 8. Polarization models of μ^1 Sco using the parameters given in Table 6 except for the inclination which has been varied from 0 to 90°. Dots are at 10° intervals of phase. The g' data points are shown on the $i = 65.4°$ plot with the dark green points being those for phase > 0.5 that fit the upper of the two intersecting loops, and the light green points being those for phase < 0.5 that fit the lower loop. In this plot, the offsets and rotation in Table 7 have been applied to the observed data points to fit the model, whereas in Fig. 4 the models were adjusted to fit the data.

This is not to imply that scattering by entrained gas is not present as a polarization mechanism in many binary systems. There is ample evidence for the presence of gas in many systems. For instance, in semidetached systems like Algol, U Sge and CX Dra, Doppler tomography has revealed the presence of gas streams and discs (Richards et al. 2000; Richards 2004, 2007). Furthermore, Piirola (1980) showed in the U Cep system the amplitude of polarization correlated with the changeable mass-transfer rate. Polarimetry is also an important tool in the study of Wolf–Rayet systems where it is used to investigate the nature and geometry of the stellar wind (St.-Louis et al. 1993; Johnson et al. 2019; Fullard et al. 2020); undoubtedly Wolf–Rayet winds are a source of polarization.

Yet, this does not rule out photospheric reflection being an important component of the total polarization in these systems. Every ordinary star in a binary will reflect light from its photosphere, and that light will be polarized, it is only the magnitude of the effect that will vary. The results presented here and in Bailey et al. (2019) suggest this could be significant. Even in WR + O systems reflection from the hot luminous photosphere of the *companion* is likely to be a significant source of polarization not presently accounted for. This has implications for the winds as well as for calculations of gas properties like the optical depth and mass, such as those of Aspin & Simmons (1982), Kemp et al. (1983), and Koch et al. (1989). Inclinations derived from gas scattering models are more robust (Berdyugin et al. 2018), since they are little effected by gas geometry. However, Ω has some weak dependence on the geometry of the scattering medium (Berdyugin et al. 2016), and given a photosphere can be approximated by a shell, an undifferentiated photospheric

Downloaded from https://academic.oup.com/mnras/article/497/2/2175/5870699 by University of Southern Queensland user on 20 June 2022

component could impact other geometrical determinations and hence Ω to a degree.

5.2 Inclination

The determination of the inclination of a binary system is important because this information is needed to measure the component masses of a double-lined spectroscopic binary. At present Stellar Population Synthesis models (e.g. Eldridge et al. 2017) are informed by very few measurements of the heaviest stars. For instance, there are only six O-type stars with mass determinations in DEBCat (Southworth 2015). Normally we require for a mass determination a double-lined binary that is also eclipsing, so that the inclination can be measured from the light-curve analysis. μ^1 Sco is an example of such a system.

However, as already discussed in Section 1, polarization observations can provide an alternate means of determining the inclination for non-eclipsing binaries and such methods are described by Rudy & Kemp (1978), Brown et al. (1978), and Aspin, Simmons & Brown (1981). However, these studies assume the polarization is due to optically thin circumstellar gas, and the *BMcLE model* in particular, which we no longer think is the correct model for μ^1 Sco, and perhaps other early-type binaries.

While μ^1 Sco has a well-determined inclination, we explored the effect on our models of varying this parameter. In Fig. 8, we show the effect on the models (plotted as a *Q–U* diagram) of changing the inclination value from 0 to 90° with all other parameters kept at their values in Table 6. This shows a number of interesting features. The largest polarization amplitude is observed for an inclination of 0° (i.e. a face-on orbit). For this orientation the degree of polarization is constant, but the polarization position angle rotates through the orbital cycle at a uniform rate. The large polarization in this case, suggests that polarization might be a way of detecting binaries which would not be detected by photometric or spectroscopic methods. Binary frequency increases with mass, and some predictions put the binary fraction for O-type stars at 100 per cent (Sana et al. 2014). Consequently, any massive apparently single star is a good target for a polarimetric companion search.

For intermediate inclinations, the *Q–U* diagrams show two intersecting loops corresponding to the two slightly unequal halves of the phase curve. The polarization amplitude varies with inclination and fits the data well for the inclination of 65.4° as given in Table 6 and used in our earlier models.

For an edge-on orbit ($i = 90°$), the polarization variation becomes a straight line in the *Q–U* plane.

We also calculated a set of models with inclination values from 61 to 69° and used these to determine the best-fitting inclination by fitting the same three-parameter model used in Table 7. Based on the g'-band data, we determine a polarimetric inclination of $63.8° \pm 2.7$, where the uncertainty is based on the same bootstrap analysis used in Section 4.2. This agrees, within the errors, with the inclination of $65.4° \pm 1.0$ (van Antwerpen & Moon 2010) and $64.4° \pm 0.3$ (Budding et al. 2015) from light-curve analysis. The precision of our measurement could probably be improved with additional observations.

6 CONCLUSIONS

We have discovered phase-locked polarization in the semietached eclipsing binary system μ^1 Sco. The initial discovery was made using a small telescope at a city-based observing site with an inexpensive instrument. This demonstrates the accessibility of polarimetry for small institutions and even amateurs.

The phase behaviour seen in μ^1 Sco is complex, and the amplitude of the signal is wavelength dependent, reaching about 700 ppm in green light, and 450 ppm in red light. We fit the polarization phase curves with a SYNSPEC/VLIDORT polarized radiative transfer model that utilizes a Wilson–Devinney geometric formalism, and as a result find that most of the polarization arises from photospheric reflection. This adds to an increasing number of other binary systems like u Her, LZ Cep, and HD 48099 where it is thought photospheric reflection could play a primary role. The agreement between the model and observations here, along with a similar result for the Spica system, leads us to conclude that polarization by this mechanism must be a common feature of early-type binaries. For more than 50 yr scattering by extra-stellar gas has been regarded as the dominant polarigenic mechanism in these systems, but this result begins to suggest a more complicated picture. It will be important to establish to what proportion gas and photospheric mechanisms each contribute in individual systems and in general. To this end we call both for more polarimetric observations of binary systems and further radiative transfer modelling to compare to historical data.

Since polarization by photospheric reflection increases with increasing temperature and reducing surface gravity, the finding has significant implications for the study of massive early-type binary systems. It provides a reliable method for the determination of inclination, and consequently mass, in non-eclipsing double-lined spectroscopic binaries, and encourages a search for missed binary companions in face-on orbits where entrained gas may not be expected. The effect will also need to be accounted for when studying winds in WR + O systems, or other close binaries polarimetrically.

ACKNOWLEDGEMENTS

This research has made use of the SIMBAD data base, operated at CDS, Strasbourg, France. This research has made use of NASA's Astrophysics Data System. We thank the former Director of the Australian Astronomical Observatory, Prof. Warrick Couch, and the current Director of Siding Spring Observatory, A/Prof. Chris Lidman for their support of the HIPPI-2 project on the AAT. We thank Prof. Miroslav Filipovic for providing access to the Penrith Observatory, and Darren Maybour for his work on its telescope, systems and assistance when observing. Fiona Lewis, Dag Evensberget, Jinglin Zhao, Shannon Melrose, and Rudy Xu also assisted with observations. Funding for the construction of HIPPI-2 was provided by UNSW through the Science Faculty Research Grants Program.

We wish to thank the referee, Andrei Berdyugin, for his contribution to improving the manuscript.

DATA AVAILABILITY

The primary data underlying this article are available in the article. Auxiliary data is available on reasonable request.

REFERENCES

AppenzellerI., HiltnerW. A., 1967, ApJ, 149, 353
AspinC., SimmonsJ. F. L., 1982, MNRAS, 199, 601
AspinC., SimmonsJ. F. L., BrownJ. C., 1981, MNRAS, 194, 283
BaileyJ., Kedziora-ChudczerL., CottonD. V., BottK., HoughJ. H., LucasP. W., 2015, MNRAS, 449, 3064
BaileyJ., CottonD. V., Kedziora-ChudczerL., 2017, MNRAS, 465, 1601
BaileyJ., Kedziora-ChudczerL., BottK., 2018, MNRAS, 480, 1613
BaileyJ., CottonD. V., Kedziora-ChudczerL., De HortaA., MaybourD., 2019, Nat. Astron., 3, 636

Downloaded from https://academic.oup.com/mnras/article/497/2/2175/5870699 by University of Southern Queensland user on 20 June 2022

BaileyJ., CottonD. V., Kedziora-ChudczerL., De HortaA., MaybourD., 2020a, Publ. Astron. Soc. Aust., 37, e004
BaileyJ., CottonD. V., HowarthI. D., LewisF., Kedziora-ChudczerL., 2020b, MNRAS, 494, 2254
BarbourM. S., KempJ. C., 1981, ApJ, 246, 203
BerdyuginA. V., 1998, Astron. Lett., 24, 84
BerdyuginA. V., HarriesT. J., 1999, A&A, 352, 177
BerdyuginA. et al., 2016, A&A, 591, A92
BerdyuginA., PiirolaV., SakanoiT., KagitaniM., YonedaM., 2018, A&A, 611, A69
BochkarevN. G., KaritskayaE. A., DoskutovV. M., SokolovV. V., 1986, Astron. Zh., 63, 71
BottK., BaileyJ., CottonD. V., Kedziora-ChudczerL., MarshallJ. P., MeadowsV. S., 2018, AJ, 156, 293
BrooksA., ClarkeD., McGaleP. A., 1994, Vistas Astron., 38, 377
BrownJ. C., McLeanI. S., EmslieA. G., 1978, A&A, 68, 415
BuddingE., ButlandR., BlackfordM., 2015, MNRAS, 448, 3784
CastelliF., KuruczR. L., 2003, in PiskunovN., WeissW. W., GrayD. F., eds, Proc. IAU Symp. 210, Modelling of Stellar Atmospheres. Astronomical Society of the Pacific, San Francisco, CA, USA, p. A20
ChandrasekharS., 1946, ApJ, 103, 351
ClarkeD., 2010, Stellar Polarimetry. Wiley-VCH, Weinheim
CollinsG. W., BuergerP. F., 1974, in GehrelsT., ed., IAU Colloq. 23: Planets, Stars, and Nebulae: Studied with Photopolarimetry, University of Arizona Press, Tucson, AZ, USA, p. 663
CottonD. V., BaileyJ., Kedziora-ChudczerL., BottK., LucasP. W., HoughJ. H., MarshallJ. P., 2016, MNRAS, 455, 1607
CottonD. V., BaileyJ., HowarthI. D., BottK., Kedziora-ChudczerL., LucasP. W., HoughJ. H., 2017, Nat. Astron., 1, 690
CottonD. V. et al., 2019, MNRAS, 483, 3636
CottonD. V., BaileyJ., HortaA. D., NorrisB. R. M., LomaxJ. R., 2020a, Res. Notes Am. Astron. Soc., 4, 39
CottonD. V., BaileyJ., PringleJ. E., SparksW. B., von HippelT., MarshallJ. P., 2020b, MNRAS, 494, 4591
DolanJ. F., 1992, ApJ, 384, 249
EddingtonA. S., 1926, MNRAS, 86, 320
EldridgeJ. J., StanwayE. R., XiaoL., McClellandL. A. S., TaylorG., NgM., GreisS. M. L., BrayJ. C., 2017, Publ. Astron. Soc. Aust., 34, e058
EritsianM. A., DocoboJ. A., MelikianN. D., TamazianV. S., 1998, A&A, 329, 1075
Espinosa LaraF., RieutordM., 2012, A&A, 547, A32
FullardA. G., St-LouisN., MoffatA. F. J., PiirolaV. E., MansetN., HoffmanJ. L., 2020, AJ, 159, 214
HandlerG., Schwarzenberg-CzernyA., 2013, A&A, 557, A1
HarringtonJ. P., 2006, Continuum Polarization Induced by Tidal Distortion in Binary Stars, https://www.astro.umd.edu/~jph/RP.pdf.
HarringtonJ. P., 2015, in NagendraK. N., BagnuloS., CentenoR., Jesús Martínez GonzálezM., eds, Proc. IAU Symp. 305, Polarimetry, Cambridge University Press, Cambridge, UK, p. 395
HubenyI., 2012, in RichardsM. T., HubenyI., eds, Proc. IAU Symp. 282, From Interacting Binaries to Exoplanets: Essential Modeling Tools, Cambridge University Press, Cambridge, UK, p. 221
HubenyI., SteflS., HarmanecP., 1985, Bull. Astron. Inst. Czech., 36, 214
JohnsonR. A., FullardA. G., LomaxJ. R., CooperK., Leon-AlvarezD., HoffmanJ. L., NordsieckK. H., 2019, Res. Notes Am. Astron. Soc., 3, 146
KempJ. C., HermanL. C., 1977, ApJ, 218, 770
KempJ. C., BarbourM. S., McBirneyR. E., RudyR. J., 1981, ApJ, 243, 557
KempJ. C., HensonG. D., BarbourM. S., KrausD. J., CollinsG. W. I., 1983, ApJ, 273, L85
KochR. H., EliasN. M., CorcoranM. F., HolensteinB. D., 1989, Space Sci. Rev., 50, 63
LunaH. G., 1988, A&AS, 74, 427
McLeanI. S., 1980, in PlavecM. J., PopperD. M., UlrichR. K., eds, Proc. IAU Symp. 88, Close Binary Stars: Observations and Interpretation. Springer, Dordrecht, The Netherlands, p. 65
MauryA. C., 1920, Harvard Ann., 84, 157
OdellA. P., 1979, PASP, 91, 326
ÖhmanY., 1934, Nature, 134, 534
PfeifferR. J., KochR. H., 1973, BAAS, 5, 345
PfeifferR. J., KochR. H., 1977, PASP, 89, 147
PickeringE. C., BaileyS. I., 1896, ApJ, 4, 235
PiirolaV., 1980, A&A, 90, 48
PressW. H., TeukolskyS. A., VetterlingW. T., FlanneryB. P., 1992, Numerical Recipes in FORTRAN. The Art of Scientific Computing. Cambridge Univ. Press, Cambridge
RichardsM. T., 2004, Astron. Nachr., 325, 229
RichardsM. T., 2007, in HartkopfW. I., HarmanecP., GuinanE. F., eds, Proc. IAU Symp. 240, Binary Stars as Critical Tools & Tests in Contemporary Astrophysics. Cambridge University Press, Cambridge, UK, p. 160
RichardsM. T., KoubskýP., ŠimonV., PetersG. J., HirataR., ŠkodaP., MasudaS., 2000, ApJ, 531, 1003
RucińskiS. M., 1966, Acta Astron., 16, 127
RudyR. J., KempJ. C., 1976, ApJ, 207, L125
RudyR. J., KempJ. C., 1977, ApJ, 216, 767
RudyR. J., KempJ. C., 1978, ApJ, 221, 200
SanaH. et al., 2014, ApJS, 215, 15
SchafferJ., 2015, Aust. J. Phil., 93, 644
SeagerS., WhitneyB. A., SasselovD. D., 2000, ApJ, 540, 504
SerkowskiK., 1965, ApJ, 142, 793
SerkowskiK., 1970, ApJ, 160, 1083
SerkowskiK., MathewsonD. S., FordV. L., 1975, ApJ, 196, 261
ShakhovskoiN. M., 1962, Astron. Zh., 39, 755
ShakhovskoiN. M., 1964, Astron. Zh., 41, 1042
ShakhovskoiN. M., 1966, Byull. Inst. Astrofiz. Akad. Nauk Tadzhik, SSR, 41–42, 69
ShakhovskoiN. M., 1969, Astron. Zh., 46, 386
SonnebornG., 1982, in JaschekM., GrothH. G., eds, Proc. IAU Symp. 98, Be Stars. Springer, Dordrecht, The Netherland, p. 493
SouthworthJ., 2015, RucinskiS.M., TorresG., ZejdaM., Living Together: Planets, Host Stars and Binaries, Astronomical Society of the Pacific Conference Sereis, volume 496, Astronomical Society of the Pacific, San Francisco, CA, USA, p. 164
SpurrR. J. D., 2006, J. Quant. Spectrosc. Radiat. Transfer, 102, 316
St.-LouisN., MoffatA. F. J., LapointeL., EfimovY. S., ShakhovskojN. M., FoxG. K., PiirolaV., 1993, ApJ, 410, 342
van AntwerpenC., MoonT., 2010, MNRAS, 401, 2059
van SmithE. P., 1956, ApJ, 124, 43
von ZeipelH., 1924, MNRAS, 84, 665
WilsonR. E., 1979, ApJ, 234, 1054
WilsonR. E., DevinneyE. J., 1971, ApJ, 166, 605

This paper has been typeset from a TEX/LATEX file prepared by the author.

Downloaded from https://academic.oup.com/mnras/article/497/2/2175/5870699 by University of Southern Queensland user on 20 June 2022